

SATURATION OF ION YIELD IN 2,2,4,4-TMP
IN RESPONSE TO VERY HIGHLY
IONIZING RADIATION

by

Myron R. Rosvick
B.Sc., University of Alberta, 1988

A Thesis Submitted in Partial Fulfillment of the
Requirements for the Degree of

MASTER OF SCIENCE

in the Department of Physics

ACCEPTED
FACULTY OF GRADUATE STUDIES

DEAN


We accept this thesis as conforming DATE _____
to the required standard

1990-01-23


Dr. R.K. Keeler, Supervisor


Dr. A. Astbury


Dr. L.P. Robertson


Dr. P. Wan


Dr. D. Axén

©MYRON RICHARD ROSVICK, 1990

University of Victoria

*All rights reserved. This thesis may not be reproduced
in whole or in part, by mimeograph or other means,
without the permission of the author.*

QC702

R68

1. 1998-1999
2. 2000-2001
3. 2002-2003
4. 2004-2005
5. 2006-2007
6. 2008-2009
7. 2010-2011
8. 2012-2013
9. 2014-2015
10. 2016-2017
11. 2018-2019
12. 2020-2021


Supervisor: Dr. Richard K. Keeler

ABSTRACT

The free ion yields in 2,2,4,4-tetramethylpentane with applied electric fields between 604 V/cm and 3625 V/cm and at three different energy depositions are found. These free ion yields are modelled using Onsager's initial recombination theory and Jaffé's column recombination theory. Onsager's theory is used to determine a voltage independent Birks factor of 0.178 ± 0.014 cm/MeV. Voltage dependent Birks factors are also determined.

Examiners:


Dr. R.K. Keeler, Supervisor


Dr. A. Astbury


Dr. L.P. Robertson


Dr. P. Wan


Dr. D. Axen

Contents

Abstract	ii
Contents	iii
Tables	v
Figures	vi
Acknowledgements	ix
1 Introduction	1
2 Theory	7
2.1 Introduction	7
2.2 The Transient Signal from the Ionization Chamber	7
2.3 Energy Deposition in TMP	13
2.3.1 Average Energy Deposition	13
2.3.2 Vavilov Distribution of Energy Deposition	20
2.4 Onsager and Jaffé theories	22
3 Experiment	26
3.1 Introduction	26
3.2 TMP and Cell Preparation	26
3.3 Beamline M11 at TRIUMF	30
3.4 Detector Telescope and Associated Electronics	33
3.5 Readout Electronics for the TMP Cell	37
3.6 Data Collection	39

4	Data Analysis	41
4.1	Data Compression	42
4.2	Kinematic Selection Criteria	42
4.3	Digital Filter Development	44
4.4	Pretrigger Selection Criteria	46
4.4.1	Initial Selection Criteria	48
4.4.2	Optimization of Selection Criteria	48
4.5	Final Model Determination	55
4.5.1	Gain vs. Voltage Correction	55
4.6	Final Peak Height Distributions	56
4.7	Errors on the Parameters	56
5	Results and Discussion	59
5.1	Free Ion Yields	60
5.2	Onsager Fits	64
5.3	Error Contributions to the Birks Factor	71
5.4	Jaffé Fits	74
5.5	Discussion of the Results	77
6	Conclusions	79
A	Current Pulse - Arbitrary Distribution with Loss	85
B	Digital Filters	92

List of Tables

3.1	Runs used in analysis.	39
5.1	Average energy deposited in the TMP for each particle/mo- mentum configuration.	60
5.2	Free ion yields and noise contributions for 400 MeV/c p's. . .	62
5.3	Free ion yields and noise contributions for 150 MeV/c π 's. . .	62
5.4	Free ion yields and noise contributions for 400 MeV/c π 's. . .	63
5.5	Zero free ion yields for the three data sets studied.	66
5.6	Voltage dependent Birks factors.	69
5.7	Birks factor error contributions.	71
5.8	Comparison of total ion yields per centimeter for Onsager and Jaffé formalism. Errors are statistical errors only.	75

List of Figures

1.1	Ionization chamber.	2
1.2	Structure of 2,2,4,4-TMP.	4
2.1	Current pulses as a function of time with $Ne/t_d \equiv 1$. The solid line represents $\tau_\ell = \infty$ and the dashed line represents $\tau_\ell = 2t_d$	9
2.2	Schematic representation of read-out electronics.	10
2.3	Theoretical response function.	12
2.4	Theoretical voltage pulse from convolution of current pulse and response function.	14
2.5	Percent multiple scattering of protons in various hydrocarbons at $E = 0.001$ MeV. The curve is a quadratic fit to the hydrocarbons represented by circles.	17
2.6	Range-energy curve for 2,2,4,4-TMP.	18
2.7	Energy loss curve for 2,2,4,4-TMP.	19
2.8	Energy loss curve for 2,2,4,4-TMP.	21
3.1	TMP cell.	27
3.2	Bell jar assembly.	29
3.3	The TRIUMF facility.	31
3.4	M11 pion channel at TRIUMF.	32
3.5	Schematic telescopic array of detectors.	33
3.6	Trigger logic and amplifier configuration.	36
3.7	Cell electronics.	37
4.1	Sample of the silicon and NaI pulse height and the Rf time-of-flight spectra. Each spectrum has the other two kinematic criteria already applied.	43

4.2	Frequency space representation of the low- and high-field current pulses and of the filter.	45
4.3	(1) A theoretical voltage pulse and (2) the corresponding digitally filtered pulse.	47
4.4	Pretrigger scatter plot showing the double lobe structure in the y-intercept data. Events in the hatched regions were rejected.	49
4.5	(1) shows the average of the pulses with low y-intercept values and (2) shows those with high y-intercept values.	50
4.6	Pretrigger selection criteria. The dashed lines represent the preliminary selection criteria and the solid lines represent the final criteria.	51
4.7	Sample of a double pulse. The tail region of the filtered pulse between $80 \mu\text{s}$ and $200 \mu\text{s}$ is fit with a straight line and pulses with high R^2 are rejected.	53
4.8	Measured response function of the electronics.	54
5.1	Sample fit of Vavilov curve with gaussian broadening for 400 MeV/c pions with an electric field of 604 V/cm on the TMP.	61
5.2	Ionization densities for constant and changing dE/dx cases. The gap in the center represents the $500 \mu\text{m}$ stainless steel electrode which also changes the dE/dx	65
5.3	Fits of G_{fi}^0 for all data sets.	67
5.4	Voltage independent Birks factor fit.	68
5.5	Voltage dependent Birks factors. The line represents the voltage independent level. The triangular points represent Aubert, et. al.'s data at $\theta = 0^\circ$	70
5.6	Plot of ion yields at limits of μ for 400 MeV/c π data.	72
5.7	Plot of ion yields at limits of τ_ℓ for 400 MeV/c π data.	73
5.8	Fit of free ion yields to Jaffé's ion recombination model.	76
A.1	Ionization chamber track orientation.	86
A.2	(a) $x > R \cos \theta$, (b) $x \leq R \cos \theta$	88
B.1	The sinusoid is sampled at equally spaced intervals. The high frequency and low frequency sinusoids will appear to be identical due to aliasing.	93

B.2	Frequency space representation of 21 point window filter (solid line) and 21 point modified window filter (dashed line).	96
B.3	Frequency space representation of 21 point window filter combined with 21 point modified window.	97
B.4	Frequency space representation of 141 point bandpass differentiator with and without Lanczos smoothing.	98
B.5	Full smoothed bandpass differentiating filter.	99

Acknowledgements

I would like to thank the many people who helped me to complete this thesis. I would like to express my deep gratitude to Paul Poffenberger for doing an enormous amount of work to get the experiment and the analysis to work as well as it did, including purifying the TMP, helping with the computer codes and fitting, and providing suggestions at key points in the analysis.

I am also very grateful to Richard Keeler for his ideas and suggestions which helped me to believe that the analysis might actually work.

I would also like to thank Richard Keeler, Margret Finke-Keeler, Paul Poffenberger, Randy Sobie, Paul Schenk, Lyle Robertson, Alan Astbury, Chris Oram, and Kate Scholberg for their untiring work during the experiment at TRIUMF.

Finally, I would like to thank my wife, Joanne, who supported me when things were getting difficult and who gave me confidence in my ability to continue.

Chapter 1

Introduction

The ion yield for single highly ionizing particles in 2,2,4,4-tetramethylpentane (TMP) has been measured using an ionization chamber. This chamber consists of a charged plate between two grounded plates with a dielectric (TMP) between them (see Fig. 1.1). A single charged particle traverses the chamber perpendicular to the plates and parallel to the electric field, ionizing the dielectric and producing pairs of positive ions and electrons which move under the influence of the electric field. Due to their lower mass, the electrons will move faster than the positive ions (typically a factor of 10^5 times faster). This motion induces a current on the charged plate which, once measured, can be used to determine the ion yield.

In practical applications, ionization chambers are components in large, total energy absorbing sampling calorimeters. This type of detector is designed to change a single high energy particle into many low energy particles which are then detected. The sampling calorimeter consists of many alternating layers of a passive absorbing material followed by the active detecting material. The absorbing material is typically uranium, lead, or iron; the

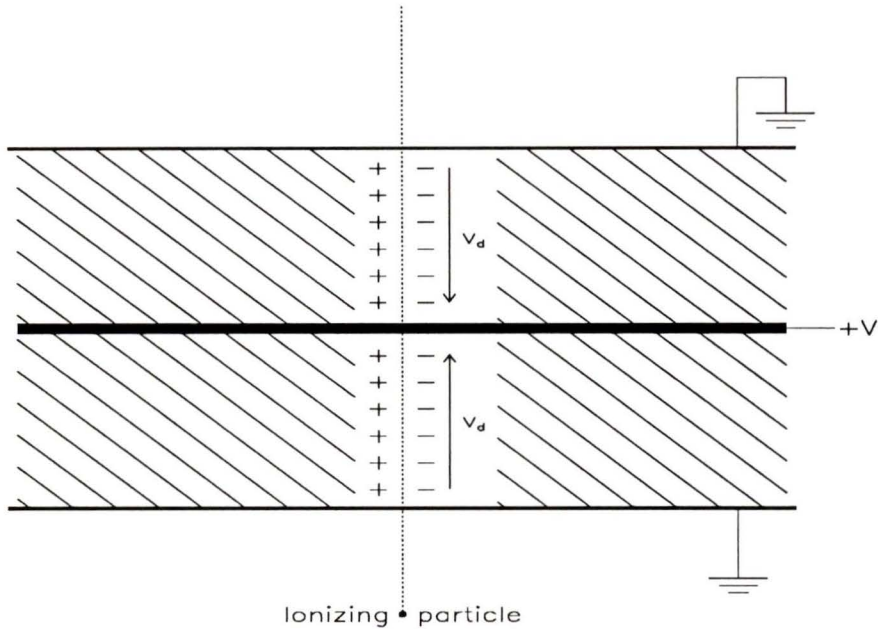


Figure 1.1: Ionization chamber.

detecting material is typically scintillator, liquid argon, or a warm liquid hydrocarbon such as TMP. This alternating layer design has the advantage of being more compact and less costly than a single thick detector made from scintillator or other material. It also allows for basic particle identification by measuring the amount of energy lost in each layer.

When a particle enters the calorimeter it will interact with an atom, creating a shower of particles which continue to interact in the detector until all of the energy is spent. The shower can consist of electromagnetic particles (electrons, positrons, and photons) and hadronic particles (all others). This causes a problem since the calorimeter will respond differently to electromagnetic and hadronic energy, reducing the resolution for detecting hadronic energy from a possible $35\%/\sqrt{E}$ to about $60\%/\sqrt{E}$. The electromagnetic

energy can be detected with good precision since electrons, positrons and photons develop a compact shower where the number of charged particles is proportional to the initial energy. Hadronic processes, however, tend to be more numerous and complicated. Interactions with a nucleus in the detector will absorb energy equal to the nuclear binding energy to split the nucleus and then produce a shower of particles. The binding energy is lost to the detector. If the response to the hadronic shower could be compensated so that the calorimeter had equal response to hadronic and electromagnetic showers ($e/h = 1$), the total energy of the incident particle could be better determined.

An incident hadronic particle will typically produce several particles, mostly π 's and nucleons, with varying energies and directions. The π^0 's will decay quickly into two photons and be detected electromagnetically. Charged hadrons (eg. pions, protons, and kaons) will ionize the material in the detector which produces a measurable signal. In materials with hydrogen, neutrons from the nuclear disintegration can collide with the free protons which ionize the active material. The number of neutrons is proportional to the binding energy of the nucleus, and so if this value can be added into the energy from the electromagnetic shower with the correct weighting, compensation can theoretically be achieved.

The specific design of the calorimeter, and in particular the material used for the active layer, will determine the weighting factor necessary. C. Rubbia [1] has proposed the use of warm liquid hydrocarbons, such as TMP (C_9H_{20} , see Fig. 1.2), since they have a large number of free protons in each molecule. They also have an additional advantage over cryogenic liquids in that they do not require expensive and bulky cooling apparatus. These liq-

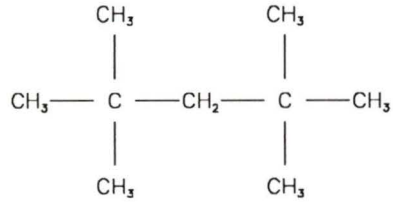


Figure 1.2: Structure of 2,2,4,4-TMP.

uids have also been shown to be radiation hard, unlike scintillators which are prone to radiation damage. The main difficulty with these liquids is that the presence of electronegative impurities at the level of a few parts per billion reduces the free electron lifetime to a point where charge collection is impractical. The UA1 group [1] has obtained lifetimes of $\geq 20\mu\text{s}$ in TMP which offered some hope of obtaining a pure enough liquid. The response of TMP to single ionizing particles must be determined in order to find the correct weighting for the saturation of the ionization due to slow protons. This response has not yet been fully measured. Wigmans [2] has performed Monte Carlo simulations of calorimeters using absorbing materials such as uranium, lead, and iron, with detector materials such as plastic scintillator, liquid argon, silicon, and TMP, to determine the e/h values and the energy resolution with each configuration. He did not have a measure of the weighting necessary for TMP (the Birks factor, kB), but approximated it with two different values: the value for a plastic scintillator ($kB = 0.014\text{cm/MeV}$) and the value for liquid argon ($kB = 0.0063\text{cm/MeV}$).

This thesis will study the saturation effects in TMP for low fields (600 to 3600 V/cm) and moderately ionizing particles. The saturation can be parameterized by the Birks factor, a parameter in a semi-empirical formula proposed by J.B. Birks [3] in 1951 to explain saturation effects in signals

from irradiated scintillating materials. This thesis will also investigate the applicability of two competing recombination theories: Onsager's[4] initial recombination theory, and Jaffé's [5] columnar recombination theory. Onsager's theory can be directly applied to the determination of the Birks factor while Jaffé's theory is in a different form, and will not give a measure of this quantity.

Chapter 2 presents the theoretical principles involved in the analysis. The signal which is expected from the ionization chamber is modelled as the convolution of the current pulse with the response of the electronics. The average energy deposition is then determined based on the Bethe-Bloch equation and parameterizations of tabulated data, and the distribution of energy loss is modelled based on Vavilov's theory. The free ion yield is determined from the energy distribution and is subsequently discussed in terms of Onsager's and Jaffé's theories.

Chapter 3 describes the ionization chamber used in the experiment and the procedures used to fill it with TMP. The beamline at TRIUMF is discussed with particular emphasis on the specific properties of interest to the experiment. These include minimum ionizing to highly ionizing pions and protons with well defined energy. The particle identification and data acquisition, involving a telescope of detectors and their associated electronics, is then presented. Finally, the readout electronics for the TMP, and the data acquisition for the experiment is discussed.

In chapter 4, the four passes used to analyze the transient signals recorded during the experiment and determine the peak height distributions are explained. A digital filter is developed to provide identification of double pulses and to reduce noise contributions to the peak height distributions. The var-

ious data selection criteria and the effects of these criteria on the fit to the electronic response function are discussed. This response function is determined and the gain corrections due to the amplification chain and the digital filter are computed. The final peak height distributions are calculated.

Chapter 5 presents the procedure used to obtain the free ion yields and discusses these results in terms of Onsager's and Jaffé's theories. The free ion yield is determined from a fit of Vavilov's theory to the peak height distributions, combined with the average energy deposited in the cell. The free ion yields are modelled with Onsager's and Jaffé's theories, and a voltage independent Birks factor is determined from Onsager's formalism. A set of voltage dependent Birks factors are also computed from the ratios of Birks equation for the different energy depositions.

Chapter 6 summarizes the results and discusses what conclusions can be drawn from them. These results are compared with previous results and some final comments are made.

Chapter 2

Theory

2.1 Introduction

The free ion yield is determined from the number of ion pairs created in the TMP per unit energy deposited by the incident charged particle. This chapter discusses the theoretical principles used to determine these properties of TMP. The current pulse which is expected from the TMP cell and the voltage pulse resulting from the convolution of this pulse with the response of the electronics are described. The mean energy deposition is determined by the Bethe-Bloch equation and published data, and fluctuations in this quantity are discussed in terms of Vavilov's theory. This is followed by a discussion of Onsager's and Jaffé's recombination theories.

2.2 The Transient Signal from the Ionization Chamber

The data to be analyzed consists of a current pulse produced by a charge distribution drifting within a liquid under the influence of an electric field.

The basic theory of the current pulse is presented in Appendix A. This analysis discusses only the case where the particle passes completely through the cell, parallel to the external electric field. The initial charge density is also assumed to be constant. This is a good approximation for the 150 and 400 MeV/c momentum pions but since the protons are more highly ionizing, they have a non-constant charge density. As will be shown later, this only amounts to a 0.04% correction since the charge distribution varies approximately linearly over the thickness of the cell. The general current pulse for a uniform charge density (Eq. A.16) reduces to

$$i(t) = \begin{cases} \frac{Ne}{t_d} \left(1 - \frac{t}{t_d}\right) e^{-t/\tau_\ell} & ; t < t_d \\ 0 & ; t \geq t_d. \end{cases} \quad (2.1)$$

where Ne is the total number of electrons produced by the passage of the incident particle, t_d is the time for an electron to drift the entire distance from the ground plate to the positive high voltage plate of the cell, and τ_ℓ defines the average rate of capture of electrons by impurities within the liquid. The applied voltage on the cell determines the drift time, t_d , by the relation

$$t_d = \frac{d}{v_d} = \frac{d^2}{\mu V} \quad (2.2)$$

where

$$v_d \equiv \mu E. \quad (2.3)$$

μ is the free electron mobility in the liquid and $E = V/d$ is the electric field, where V is the applied voltage and d is the thickness of the cell. Fig. 2.1 shows this current for values of $\tau_\ell = \infty$ and $\tau_\ell = 2t_d$.

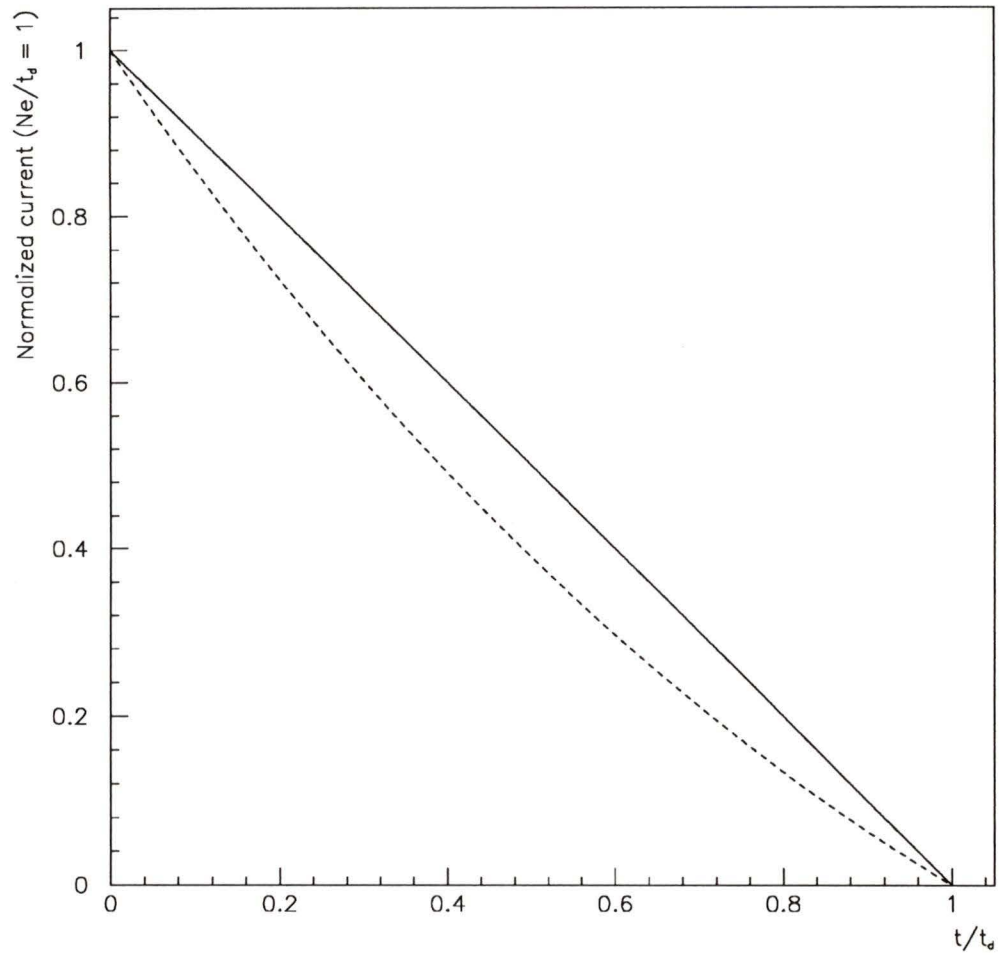


Figure 2.1: Current pulses as a function of time with $Ne/t_d \equiv 1$. The solid line represents $\tau_\ell = \infty$ and the dashed line represents $\tau_\ell = 2t_d$.

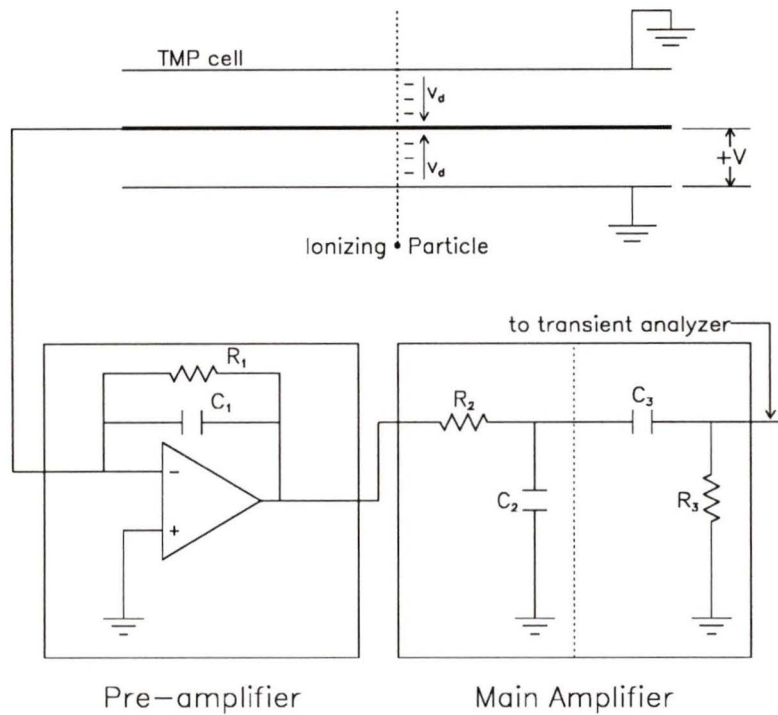


Figure 2.2: Schematic representation of read-out electronics.

The voltage pulse is the convolution of the current pulse with the electronics response function. This function represents the response of the electronics (shown schematically in Fig. 2.2) to an input delta function. There is a preamplifier attached directly to the cell electrode which can be modelled as an integrating op-amp. Ideally, the op-amp will have zero rise time and a decay time given by $\tau_1 = R_1 C_1$. The main amplifier follows the preamplifier and can be modelled as an RC integrator ($\tau_2 = R_2 C_2$) followed by an RC

differentiator ($\tau_3 = R_3 C_3$). The model used is

$$h(t) = \frac{G}{C_{fb}} \sum_{i=1}^3 A_i e^{-t/\tau_i}. \quad (2.4)$$

with the constants A_i given by circuit theory as,

$$A_i = \frac{\tau_1 \tau_3}{(\tau_i - \tau_{i-1})(\tau_i - \tau_{i+1})} ; i = 1, 2, 3 \text{ (cyclic permutation)}$$

where C_{fb} is the feedback capacitance in the preamplifier and G is the gain of the amplifier. Fig. 2.3 shows the shape of this function for typical values of the time constants. The voltage is then given by

$$v(t) = \int_0^t h(t-x)i(x) dx. \quad (2.5)$$

An input current delta function can be produced by applying a step voltage, V_{in} , to a test capacitor, C_{Test} . This produces $i(t) = Ne_{Test} \delta(t)$, where $Ne_{Test} = V_{in} C_{Test}$, and gives

$$v(t) = \frac{GNe_{Test}}{C_{fb}} \sum_{i=1}^3 A_i e^{-t/\tau_i} \quad (2.6)$$

which can be used to find the response function parameters. For the current pulse given by Eq. 2.1, the voltage pulse is

$$v(t) = \begin{cases} \frac{GNe}{C_{fb}} \sum_{i=1}^4 \frac{A_i}{(\xi_i t_d)^2} \left\{ e^{-t/\tau_i} [1 + \xi_i(t_d - t)] - e^{-t/\tau_i} (1 + \xi_i t_d) \right\} & t < t_d \\ \frac{GNe}{C_{fb}} \sum_{i=1}^4 \frac{A_i}{(\xi_i t_d)^2} \left\{ e^{\xi_i t_d - t/\tau_i} - e^{-t/\tau_i} (1 + \xi_i t_d) \right\} & t \geq t_d \end{cases} \quad (2.7)$$

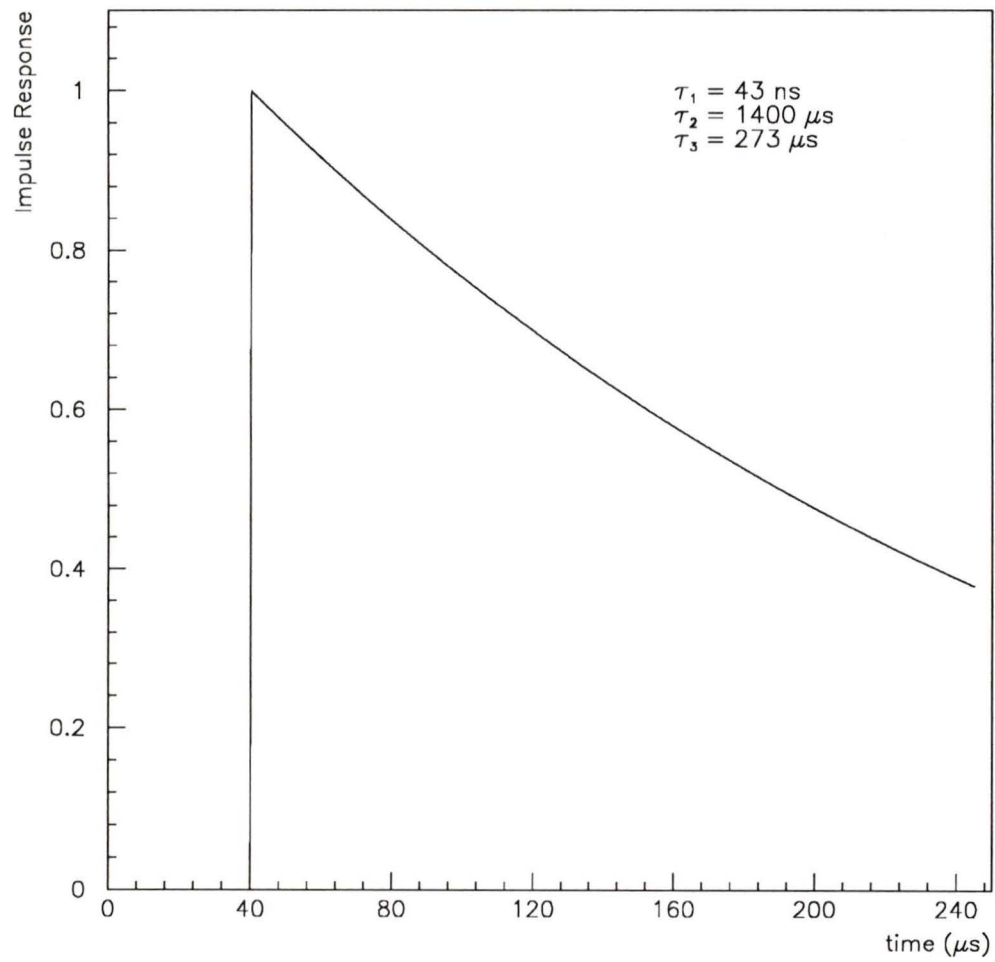


Figure 2.3: Theoretical response function.

where

$$\xi_i = \frac{\tau_\ell - \tau_i}{\tau_\ell \tau_i}. \quad (2.8)$$

Fig. 2.4 shows this function for typical parameter values.

2.3 Energy Deposition in TMP

2.3.1 Average Energy Deposition

In order to obtain meaningful results from the data, we need to know the energy deposited in the cell, and therefore the initial energy of the incident particle as it enters the cell. This involves a detailed knowledge of not only the incident beam energy, but the energy lost in each of the upstream detectors. The average energy loss is determined from the Bethe-Bloch equation, given as

$$-\frac{dE}{dx} = 2\pi N_a r_e^2 m_e c^2 \rho \frac{Z}{A} \frac{z^2}{\beta^2} \left[\ln \left(\frac{2m_e \gamma^2 v^2 W_{\max}}{I^2} \right) - 2\beta^2 - \delta - 2\frac{C}{Z} \right], \quad (2.9)$$

where r_e is the classical electron radius, m_e is the electron mass, $N_a = 6.022 \times 10^{23}$ cm is Avogadro's number, c is the speed of light in a vacuum, ρ is the density of the absorbing material, Z is the atomic number of the absorbing material, A is the atomic weight of the absorbing material, z is the charge of the incident particle, v is the velocity of the incident particle, $\beta = v/c$ of the incident particle, $\gamma = 1/\sqrt{1-\beta^2}$, W_{\max} is the maximum energy transfer allowed in a single collision, I is the mean excitation potential, δ is the density correction, and C is the shell correction. For an incident particle of

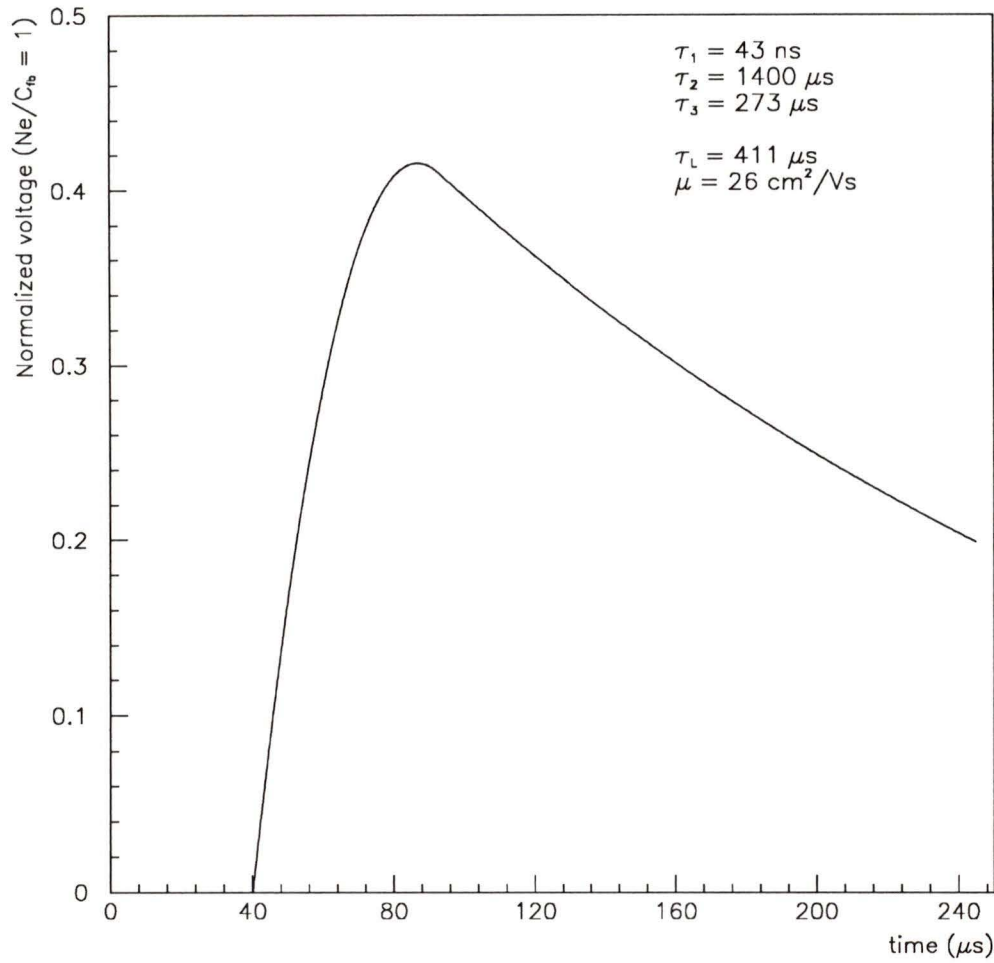


Figure 2.4: Theoretical voltage pulse from convolution of current pulse and response function.

mass M , kinematics gives

$$W_{\max} = \frac{2m_e c^2 \eta^2}{1 + 2s\sqrt{1 + \eta^2} + s^2},$$

where $s = m_e/M$ and $\eta = \beta\gamma$. J.F. Janni [6] has performed detailed calculations of the Bethe-Bloch equation, including the higher order density and shell corrections, for various materials. His calculations produced range and energy loss values for protons with initial kinetic energies between 10^{-3} MeV and 10^4 MeV in logarithmically increasing intervals.

The tables did not include values for TMP, necessitating the use of the following approximation. The energy losses of carbon and hydrogen were combined in the approximate relation for compounds

$$\frac{dE}{dx} = \sum_i \left\{ \frac{1}{\rho_i} \frac{dE}{dx} \right\} \quad (2.10)$$

with the summation over the individual elements in the compound, and ρ_i being the percent by weight of each element. Using this energy loss, the pathlength of protons in TMP was calculated by integrating

$$P(E) = P(E_0) + \int_{0.001}^E \left(\frac{dE'}{dx} \right)^{-1} dE'. \quad (2.11)$$

$P(E_0)$ is a zero point value that had to be added since Janni's tables only went to 0.001 MeV. This method was tested on silicon (which was in Janni's tables) and found to be in excellent agreement. The zero point was not known for TMP, but was approximated by noting that

$$P(E) \approx \frac{\Delta E}{dE/dx} \quad (2.12)$$

with dE/dx given in Eq. 2.10. Using $\Delta E = 0.001$ MeV and the corresponding dE/dx , the zero point was found to be $P(E_0) = 0.005$ mg/cm³. Again, this method was tested on CH₂ and found to agree with Janni's value to about 2%.

The pathlength, however, is not the true range of the particle in the material. Multiple scattering within the material will cause the pathlength to be longer than the actual distance that the particle travels in the incident direction. The range and pathlength are related by

$$R(E) = (1 - \kappa(E))P(E) \quad (2.13)$$

where $\kappa(E)$ is the percent multiple scattering which is included in Janni's tables. The multiple scattering for TMP was found by interpolating between isobutane and polyethylene. These two were chosen because they had the closest percentages of carbon to that of TMP. Fig. 2.5 shows a plot of the percentage of carbon by weight of various hydrocarbons, including TMP, against the percent multiple scattering of protons with 0.001 MeV energy to illustrate the accuracy of this method. From the quadratic fit plotted, the discrepancy in the value for TMP will be less than 0.5%. The resulting energy loss and range curves are shown in Figs. 2.6 and 2.7.

In order to determine the total energy loss in each of the telescope elements (scintillators, silicon (Si), sodium iodide (NaI), Mylar, air, aluminum, steel and TMP), a 19th order Chebyshev polynomial was fitted to both the range and the energy loss curves of each. Comparison of the fitted curves and the tables showed that within the energy ranges used in the experiment, there was less than 1% error. A *regula falsi* form of Newton's iterative method was then used to invert the fit to determine the energy at a given range. The

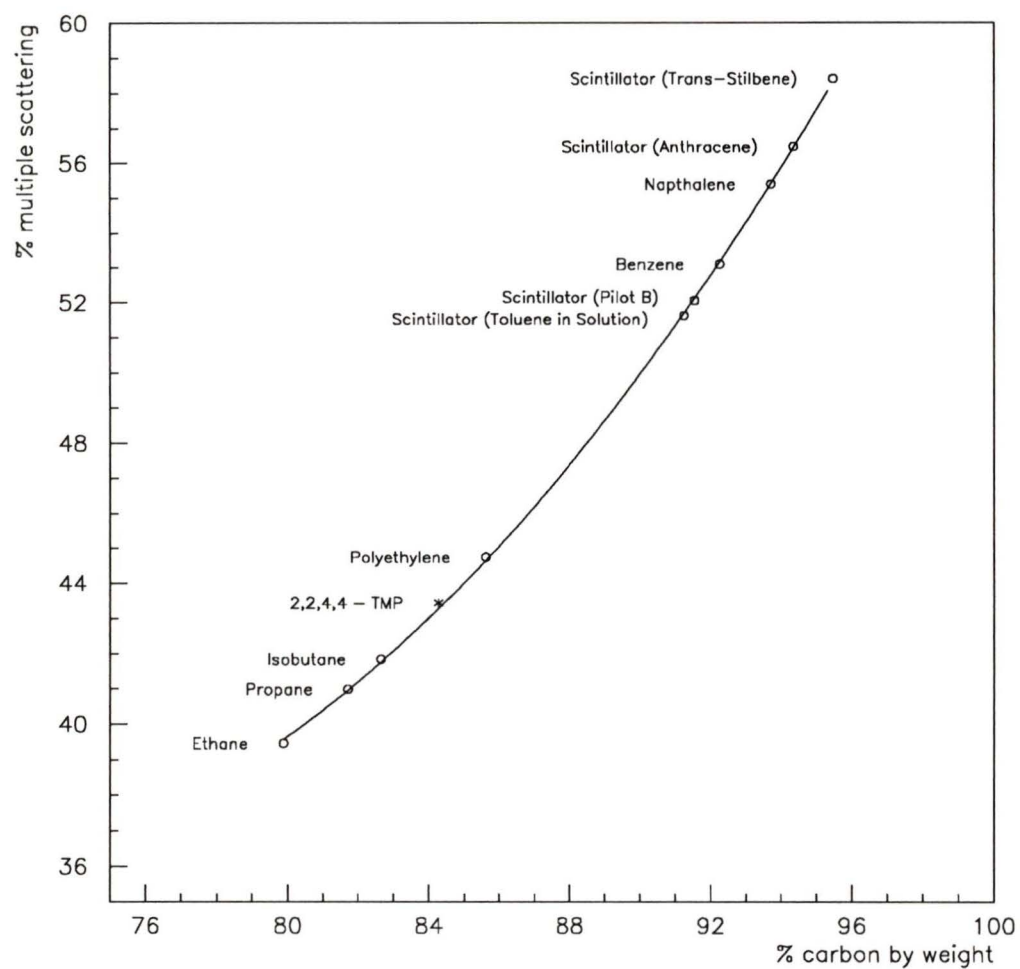


Figure 2.5: Percent multiple scattering of protons in various hydrocarbons at $E = 0.001$ MeV. The curve is a quadratic fit to the hydrocarbons represented by circles.

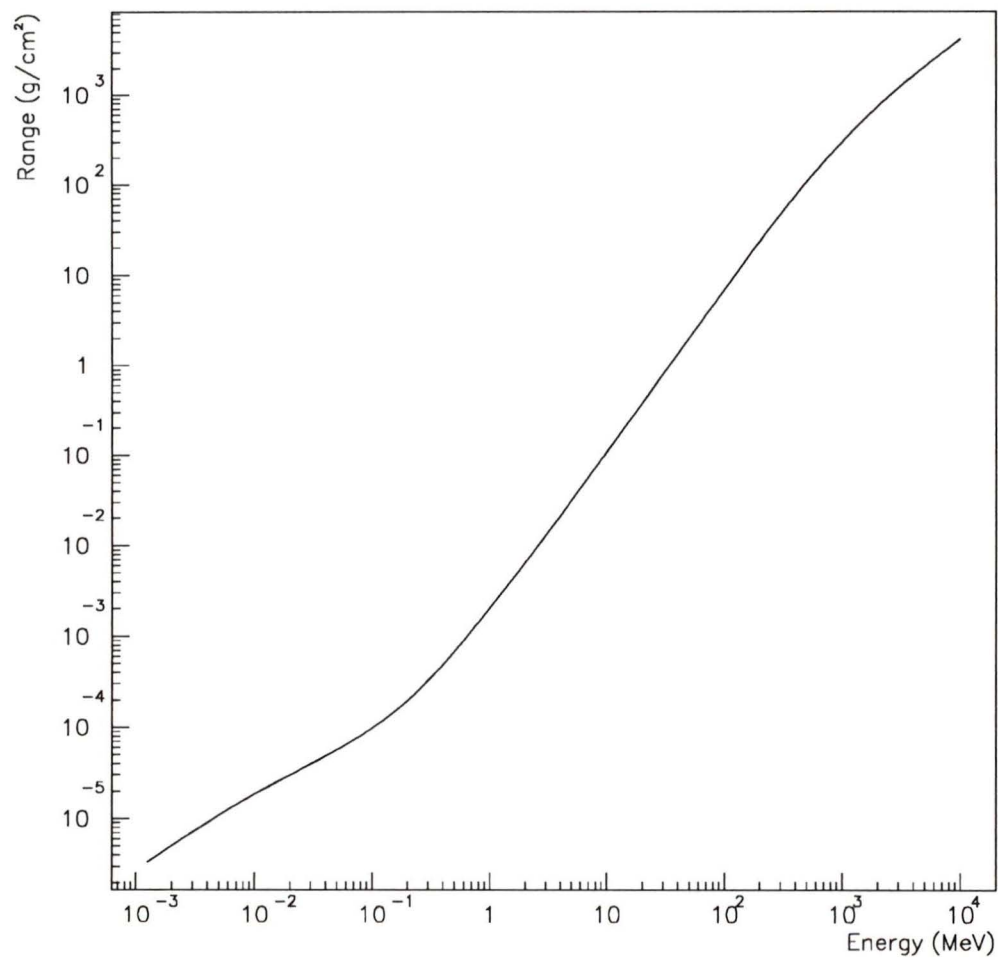


Figure 2.6: Range-energy curve for 2,2,4,4-TMP.

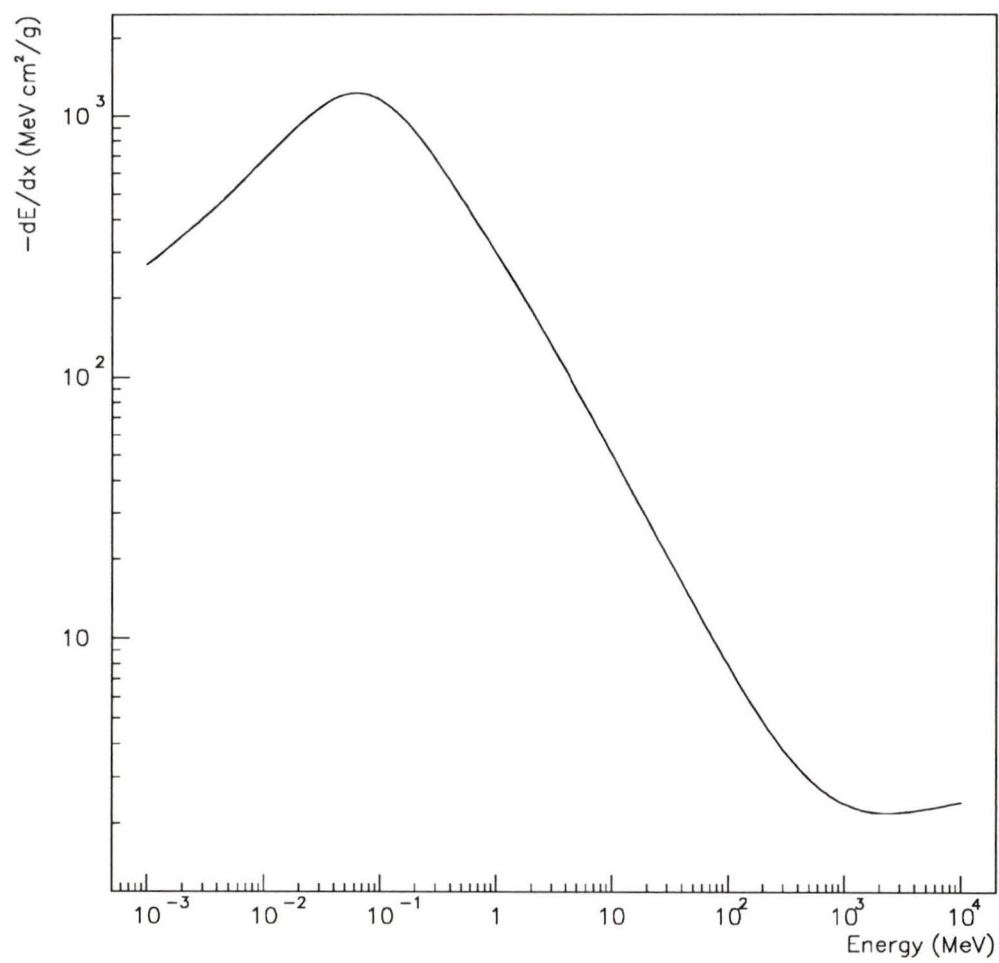


Figure 2.7: Energy loss curve for 2,2,4,4-TMP.

final calculation of all energy losses in the telescope was used to determine the (nominal) incident particle energy at the cell and the total energy loss within the cell.

2.3.2 Vavilov Distribution of Energy Deposition

Due to statistical fluctuations in the energy loss in a target, the amount of energy deposited is not distributed in a gaussian about the mean energy loss. Landau [7] determined a mathematical form describing the distribution for thin absorbers. He assumed that the cross-section for a particle interacting with the material and losing a given amount of energy was inversely proportional to the initial energy. He then integrated over $E = [0, \infty]$ to obtain the distribution of the energy loss. Vavilov [8] modified this treatment to apply to thick targets by only integrating to W_{\max} . These two distributions are shown in Fig. 2.8. For the energies considered in this analysis, Vavilov's theory is more applicable. This theory defines a variable λ which can be expressed as

$$\lambda = (\Delta E - \langle \Delta E \rangle) / W_{\max} - \kappa(1 + \beta^2 - \gamma) \quad (2.14)$$

where ΔE is the actual energy loss, $\langle \Delta E \rangle$ is the average energy loss, W_{\max} is the maximum kinematically allowed energy transfer, κ is the ratio of ξ / W_{\max} , $\xi = 0.0637x / \beta^2$ MeV for x cm of TMP, β^2 is the ratio of v/c for the incident particle, and γ is Euler's constant (0.577215...). A computer code developed at CERN [9], with input parameters λ , κ , and β^2 , was used to calculate the Vavilov distribution in λ and then Eq. 2.14 was used to convert to ΔE .

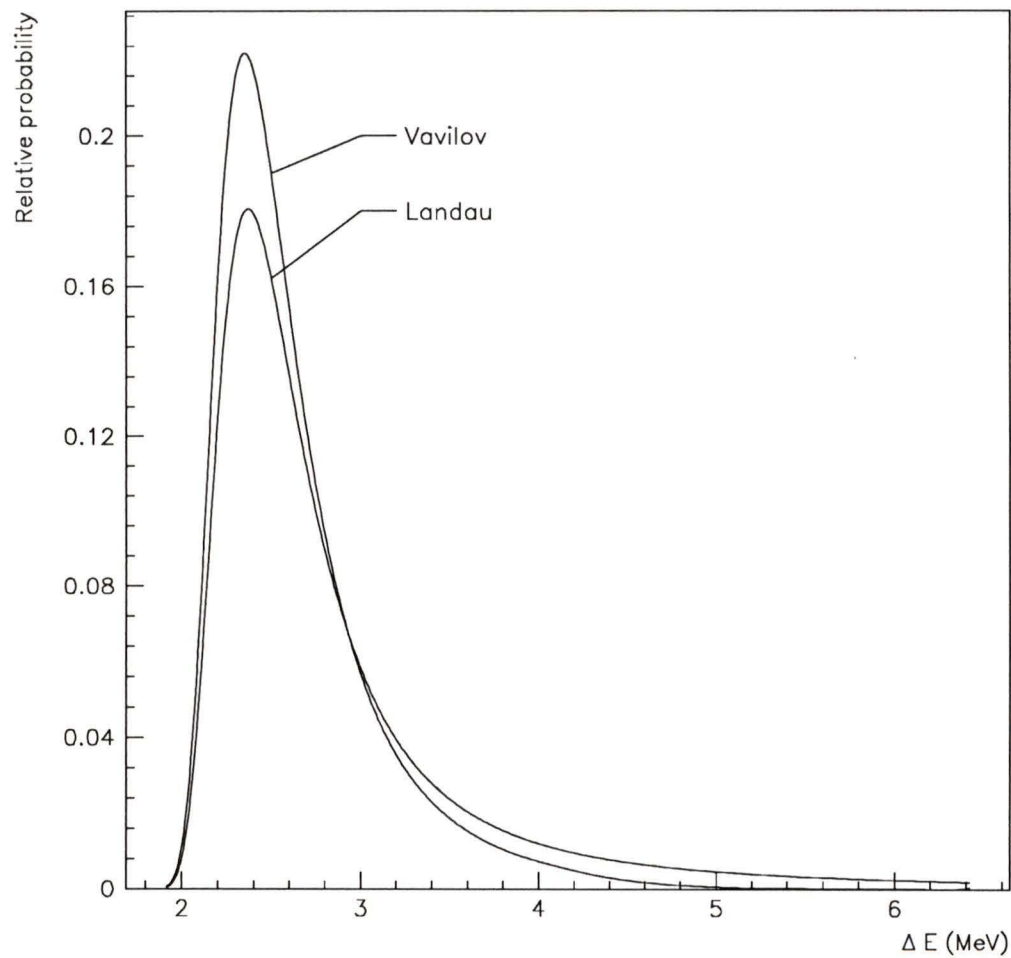


Figure 2.8: Energy loss curve for 2,2,4,4-TMP.

2.4 Onsager and Jaffé theories

Comparing the Vavilov curve, broadened by a gaussian for electronic noise, to the measured distribution of deposited energy, one can extract the free ion yield (G_{fi}). This is a parameter describing the number of electrons which escape recombination with their parent ions and drift to the high voltage electrode creating the current pulse described above. The peak height of each pulse is directly related to the energy deposited in the TMP through the relation $N = G_{\text{fi}} \Delta E$ (N is the number of counts at the peak). The free ion yield has been modelled in two ways.

Onsager developed a theory which describes the probability of a positive and a negative ion not recombining while in the field of each other and in an external electric field while undergoing Brownian motion. He determined the probability to be

$$\phi(r, \theta) = e^{-r_c/r - \beta(1 + \cos \theta)} \sum_{j,m=0}^{\infty} \frac{\beta^{j+m} (1 + \cos \theta)^{j+m} r_c^j r^m}{j!(j+m)!}, \quad (2.15)$$

where $r_c = e^2/4\pi\epsilon_0\epsilon k_B T$, $\beta = eE/2k_B T$, ϵ is the dielectric constant of the material, and θ is the angle between the electric field and a line joining the positive and negative ion pair. At zero field, this result reduces to a simple exponential

$$\phi(r, \theta) = e^{-r_c/r}.$$

G.R. Freeman [10] showed that if the ion pairs are isotropically oriented about the direction of the field, this result must be averaged over all θ giving

$$\phi(r) = e^{-r_c/r} (1 + \beta r_c + 0.375\beta^2 r_c^2 - 0.750\beta^2 r_c r + \dots). \quad (2.16)$$

The free ion yield in a material is proportional to this probability convoluted with the initial distribution of the positive and negative ions, $F(r)$, giving

$$G_{\text{fi}}^E = G_{\text{tot}} \int_0^{\infty} F(r) \phi(r) dr \quad (2.17)$$

where G_{tot} is the total number of ions/100 eV produced by the ionization. This leads to the equation

$$\frac{G_{\text{fi}}^E}{G_{\text{fi}}^0} = 1 + \frac{9.690E}{\epsilon T^2} + \frac{35.21E^2}{\epsilon^2 T^4} - \frac{4.214 \times 10^4 E^2}{\epsilon T^3} \frac{\int_0^{\infty} F(r) e^{-rc/r} r dr}{\int_0^{\infty} F(r) e^{-rc/r} dr} + \dots \quad (2.18)$$

Under the assumption that the initial distribution is given by

$$F(r) = \frac{4r^2}{\sqrt{\pi} b^3} e^{-r^2/b^2} \quad (2.19)$$

where b is the dispersion parameter, the integrals in the last term on the right side of Eq. 2.18 can be numerically integrated. For an assumed value of $b = 158 \text{ \AA}$ [11], the denominator is 0.19492 and the numerator is 43.689 \AA giving the ratio as 224.14 \AA . Note that the denominator of the ratio is the integral in Eq. 2.17 for $E = 0$, giving approximately 5 times more ions produced than are collected at zero field.

Onsager's theory allows a simple method for determining the Birks factor of a liquid. This factor appears in Birks' semi-empirical relation

$$\frac{dI}{dx} = \frac{c(dE/dx)}{1 + kB(dE/dx)} \quad (2.20)$$

where kB is the Birks factor and dI/dx is the amount of ionization produced per cm. Given that the free ion yield can be represented by the ratio of

dI/dx over dE/dx , Birks' equation can be rewritten as

$$G_{\text{fi}} = \frac{A}{1 + kB(dE/dx)} f(E) \quad (2.21)$$

where $f(E)$ is given by the right side of Eq. 2.18.

Jaffé treated the ionization as a column of charge which was governed by the relation

$$\frac{\partial n_{\pm}}{\partial t} = D_{\pm} \left(\frac{\partial^2 n_{\pm}}{\partial x^2} + \frac{\partial^2 n_{\pm}}{\partial y^2} \right) \mp \mu_{\pm} E \sin \theta \frac{\partial n_{\pm}}{\partial x} - kn_+n_-. \quad (2.22)$$

D_{\pm} is the diffusion constant, n_{\pm} is the ion concentration, μ_{\pm} is the mobility of the ions in the material, θ is the angle between the field and the ionization track, and k is the recombination rate constant. Jaffé assumed that the recombination was initially less important than the diffusion and proceeded to derive a relation for the fraction of ions that escape recombination. For angles greater than about 10° , his result is approximately

$$\frac{G_{\text{fi}}^{E,\theta}}{G_{\text{tot}}} \simeq \frac{1}{1 + \alpha \sqrt{(\pi/Z)S(Z)}} \quad (2.23)$$

where

$$\alpha = r_c N_0, \quad (2.24)$$

$$S(Z) = \frac{1}{\sqrt{\pi}} \int_0^\infty \frac{e^{-s} ds}{\sqrt{s(1 + s/Z)}}, \quad (2.25)$$

and

$$Z = \frac{E^2 \sin^2 \theta (\mu_+ + \mu_-)^2 (b_+^2 + b_-^2)}{4(D_+ + D_-)^2} \quad (2.26)$$

N_0 is the initial ion density and b_{\pm} is again the dispersion parameter which also represents the initial radius of the positive/negative ion distribution. For $\theta = 0^\circ$, Jaffé's exact solution is

$$\frac{G_{\text{fi}}^{E,0}}{G_{\text{tot}}} = \frac{e^{-1/\alpha}}{\alpha\beta} \{E_i[1/\alpha + \ln(1 + \beta)] - E_i(1/\alpha)\} \quad (2.27)$$

with

$$\beta = \frac{4(D_+ + D_-)L}{E(b_+^2 + b_-^2)(\mu_+ + \mu_-)} \quad (2.28)$$

and E_i is the exponential integral. It is clear that this form will not easily reduce to the form of Birks' equation, even though Eq. 2.23 will. Since this thesis will only deal with the $\theta = 0^\circ$ case, a Birks factor determination will not be possible within Jaffé's framework.

In 1952, H.A. Kramers proposed a small modification to Jaffé's theory which should be more applicable to liquids, since it initially ignores the diffusion term in Eq. 2.22 instead of the recombination term. The resulting form gives

$$\frac{G_{\text{fi}}^{E,\theta}}{G_{\text{tot}}} = \frac{2N_0f}{\sqrt{\pi}} \int_0^\infty \frac{\sqrt{x} dx}{fe^x + 1} \quad (2.29)$$

where

$$f = \frac{\epsilon b E \sin \theta}{2\sqrt{\pi} e N_0}. \quad (2.30)$$

This equation reduces to zero at $\theta = 0^\circ$ and so is not analyzable in this thesis. This result can be seen in Eq. 2.22 since at $\theta = 0^\circ$, the electric field dependence drops out, and since the diffusion is being neglected to first order we would have full recombination.

Chapter 3

Experiment

3.1 Introduction

This chapter describes the procedures used to purify the TMP and to clean and fill the cell with the liquid. The M11 beamline at TRIUMF and the detector telescope placed in the beam are then discussed. The data acquisition trigger and the readout electronics for the scintillators are presented followed by a description of the amplification chain for the TMP signals. Finally, the data collection during the experimental run is described.

3.2 TMP and Cell Preparation

The initial concern in the preparation of the TMP was to be sure the liquid was as pure as possible. This required a two stage procedure: the TMP itself must be purified to a high degree, and the cell must be very clean to reduce additional contamination. The purification procedure involved evaporating the TMP through molecular sieve and condensing it in a glass cell to await transfer to the metal cell used in the experiment. The purification

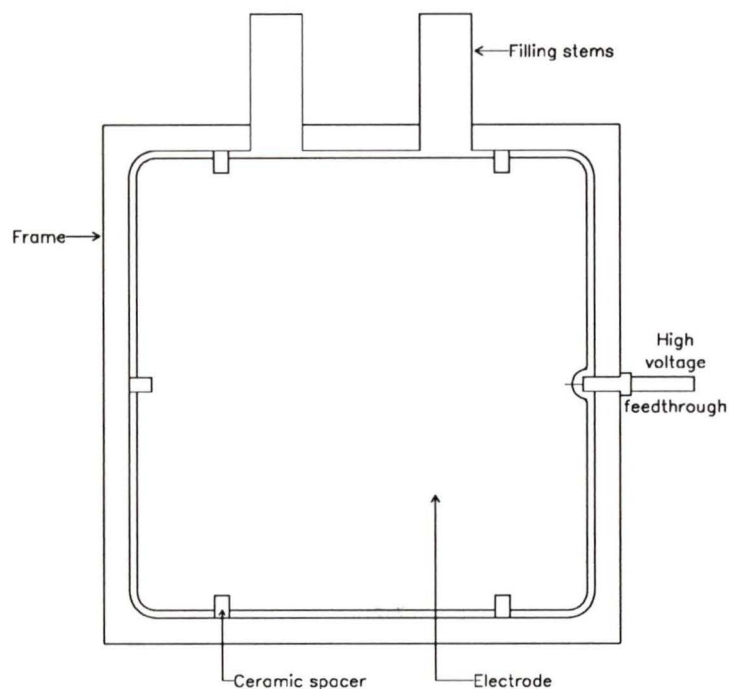


Figure 3.1: TMP cell.

is explained in detail in the M.Sc thesis by Li [12]. The TMP was tested for purity by observing that cosmic ray signals were produced in the liquid while it was still in the glass cell.

The cell used in this experiment was constructed at CERN and is shown in Fig. 3.1. The cell was 1.735 cm thick with 0.015 cm thick stainless steel walls. The thin walls provided minimal degradation of the energy of the incident particle while still providing safe containment of the liquid. The walls contained 1.655 cm of TMP which was divided in half by a 0.050 cm stainless steel central electrode. The electrode was separated from the frame of the cell by ceramic spacers so that the frame could be grounded while voltage was being supplied to the electrode. The two filling stems were

1.0 cm diameter openings, large enough to allow for efficient evacuation of the cell. The high voltage feedthrough was isolated from the frame by a ceramic tube.

Cleaning the metal cell was a three stage cycle, repeated ten times at each stage. The cell was filled with 95% ethanol, agitated, and then drained to clean off any contaminants which may have accumulated from exposure to open air. After ten repetitions, the cell was filled with boiling distilled water, agitated, and drained. After another ten repetitions, the cell was placed in a heat bath and filled with boiling nanopure water, left for a few minutes, and then drained. After the final draining of the nanopure water, the cell was placed in the heat bath and warm dry nitrogen gas passed through for a half hour to dry the interior while preventing significant contamination. A similar procedure was followed to clean the tubes and pipes of the vacuum assembly.

The cell then had to be evacuated in order to assure the purity of the liquid. Due to the thin metal walls of the cell, the evacuation had to take place in a low pressure environment. This was attained by building a metal bell jar assembly (Fig. 3.2) with attachments to allow for evacuation and filling of the cell. During the preliminary vacuum testing of the system, the cell was disconnected and all valves except valve 3 were closed. A diffusion pump provided the vacuum for the bell jar while the vacuum for the cell was provided by two sorbtion pumps followed by two ion pumps. The sorbtion pumps brought the system down to about 0.1 Torr at which point they would be closed off and the ion pumps opened to the system. Once the system was verified leak free, the metal cell was connected with valves 6 and 7 open and was wrapped with thermal tape. The bell jar was then evacuated to

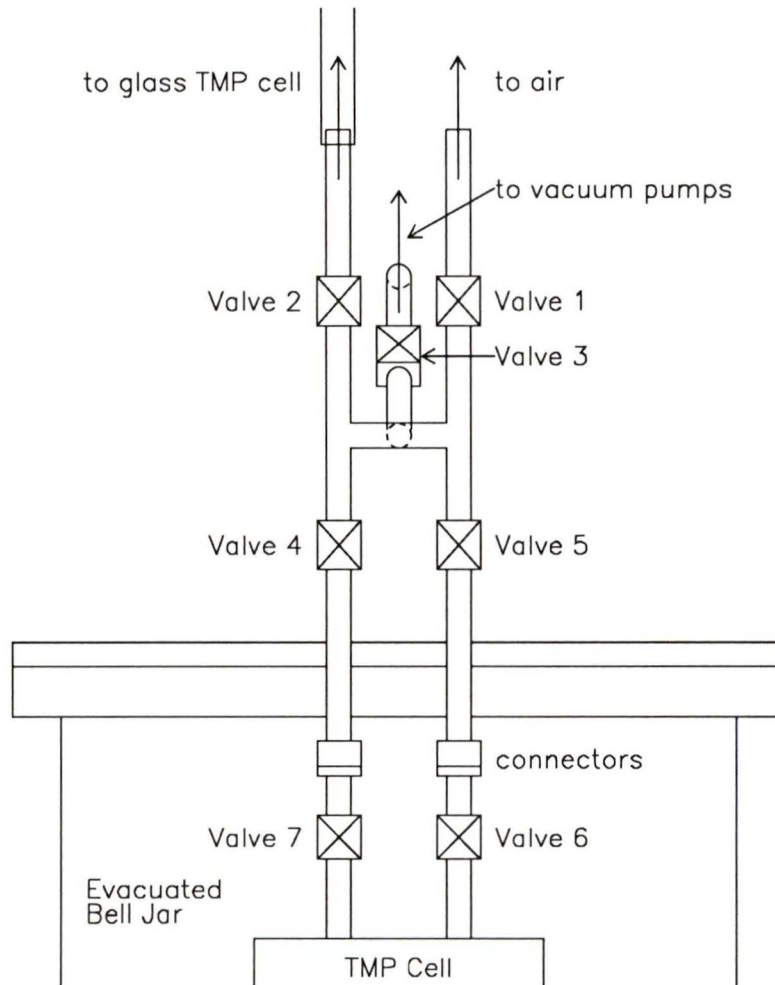


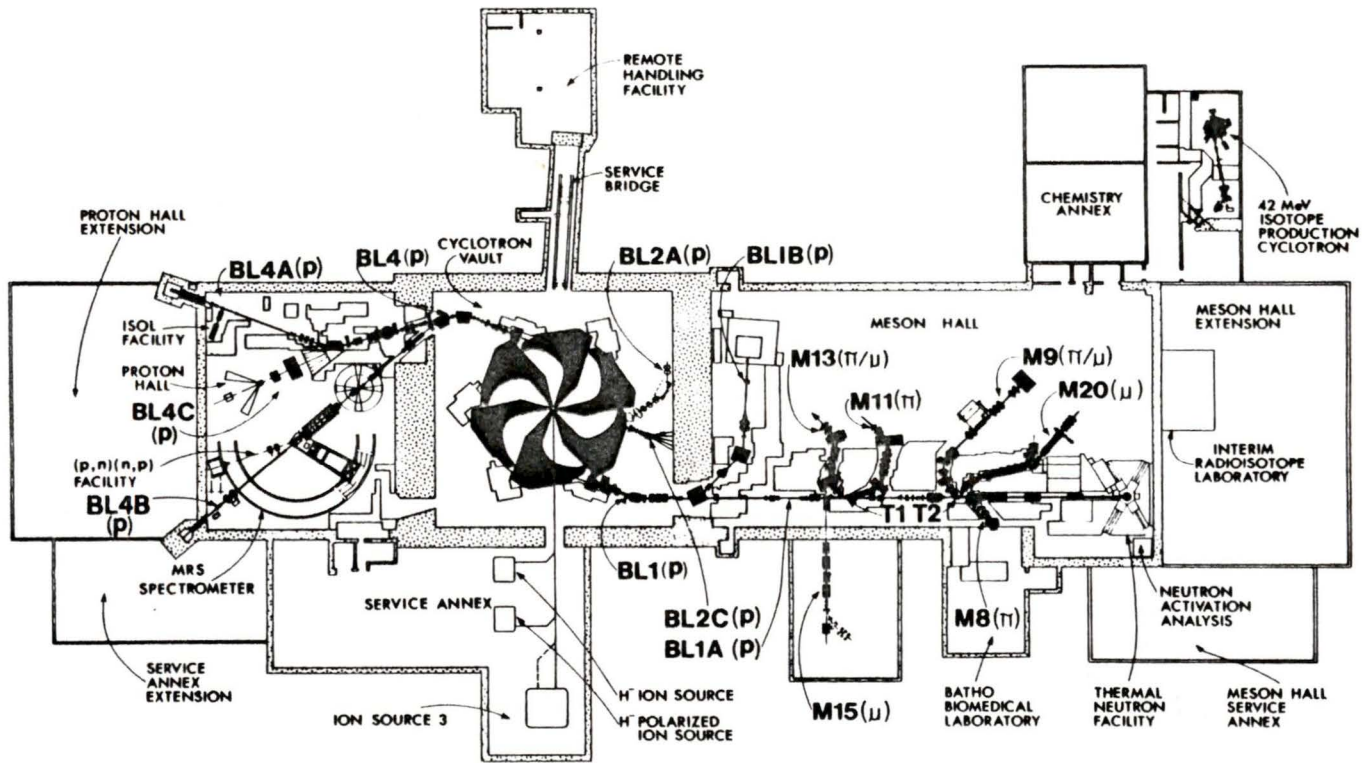
Figure 3.2: Bell jar assembly.

10^{-6} Torr. Valves 4 and 5 were opened and the system was evacuated. All of the metal tubing was wrapped in thermal tape and baked to 200 °C. The cell was baked to 300 °C to provide a temperature differential which would force any contaminants out to the relatively cooler metal tubes above the cell. The cell was eventually evacuated to 10^{-8} Torr. After several days at this pressure, valve 3 was closed and the glass cell containing the purified TMP was attached above valve 2. This valve was then opened to allow the TMP to drop into the metal cell. The valve was then closed and the vacuum was released from the bell jar. Valves 6 and 7 were closed and the TMP cell was disconnected. The TMP was again tested to be sure that a signal was seen from cosmic rays passing through the cell.

3.3 Beamline M11 at TRIUMF

The general layout of the beamlines at TRIUMF is shown in Fig. 3.3. In the main cyclotron, bunches of H^- ions are accelerated up to 520 MeV and then the electrons are stripped off by thin foils, leaving protons which are magnetically separated. These bunches are typically 3-4 ns long and are 43 ns apart. For this experiment, they were then directed down beamline BL1A and into the M11 channel (see Fig. 3.4). The average current in this beamline during the experiment was 150-200 nA. Pions which are produced in the target T1 and inelastic protons which are scattered from this target pass through quadrupole, 1AQ9, which separates these particles horizontally, and then through the septum magnet, S1, which separates them further and bends the beam away from the primary channel. The dipole magnet B1 bends the beam by an additional 60°. During pion runs, proton contamination is

Figure 3.3: The TRIUMF facility.



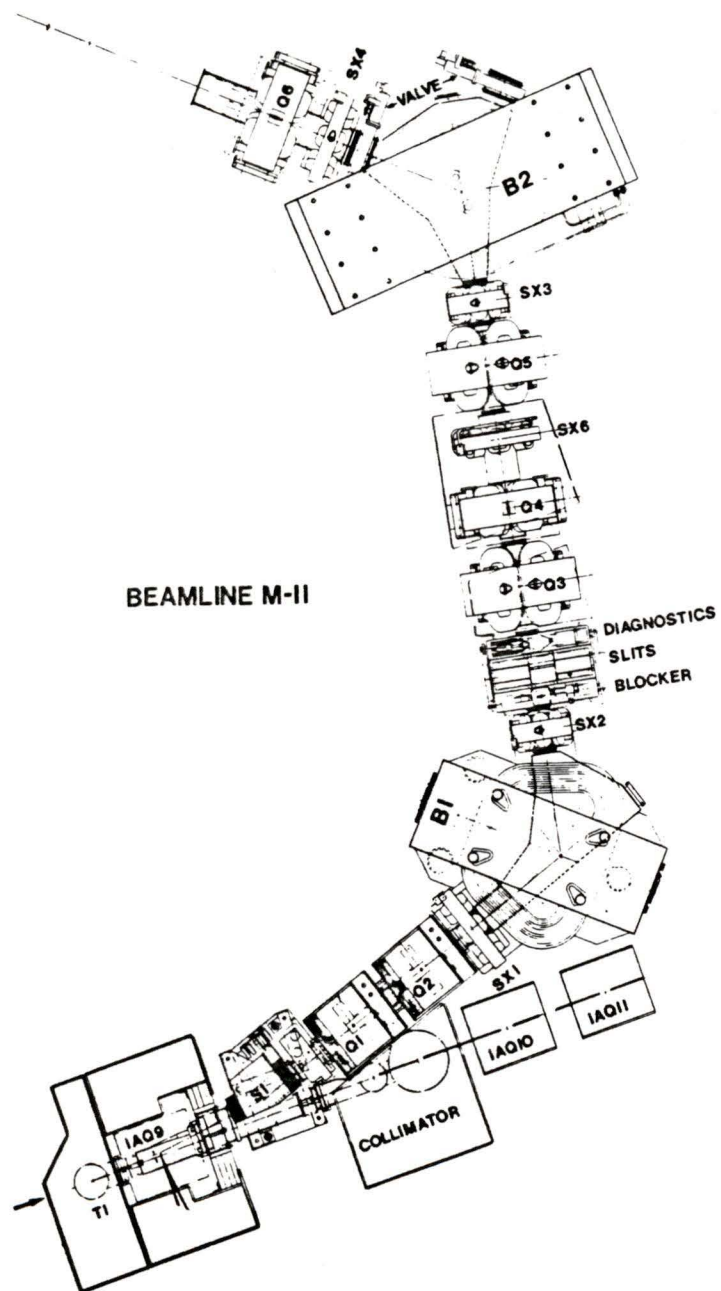


Figure 3.4: M11 pion channel at TRIUMF.

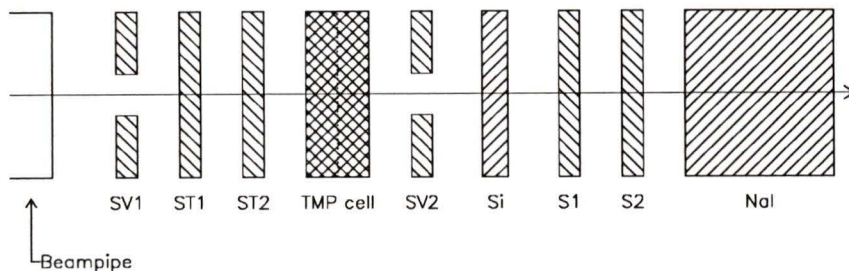


Figure 3.5: Schematic telescopic array of detectors.

reduced by the use of CH₂ absorbers (0.010 to 0.723 inches thick) located at the midplane which will differentially degrade the momenta of the pions and protons. The dipole B2 can then be used to select either the pions or protons based on their momenta. The fields in the two dipoles were independently measured by NMR probes. The field in B1 determined the momentum of the particles by the relation

$$P = \{[0.03255 (\text{B1 Magnetic Field in Gauss}) - 0.26]\} \pm 0.25\% \text{ MeV}/c.$$

3.4 Detector Telescope and Associated Electronics

The experimental telescope is shown in Figure 3.5. The counters were aligned and were surveyed before and after the run. The elements of the detector telescope upstream of the TMP cell were kept to a minimum thickness in order to have less degradation of the incident beam energy, providing a more accurate determination of the energy deposited in the cell. Thus, the end of the beampipe was covered by a 25 μm thick Kapton window which accounted for a maximum of 0.03 MeV energy loss for 400 MeV/c protons. All NE110 plastic scintillators were covered with 500 μm thick Mylar. The first veto

counter, SV1, was a $7.62 \text{ cm} \times 15.24 \text{ cm} \times 0.635 \text{ cm}$ NE110 scintillator, 1.8 cm from the end of the beam pipe, and with a 2.54 cm hole in the centre. This was followed by two very thin $10.16 \text{ cm} \times 10.16 \text{ cm}$ plastic scintillators, ST1 and ST2, which were 0.0381 cm and 0.0254 cm thick, respectively. ST1 was 2.8 cm from the end of the beam pipe and ST2 was 1.5 cm from ST1. The energy lost in each of these counters for 400 MeV/c protons was 1.4 MeV and 1.3 MeV, respectively. The total energy lost in the upstream elements was approximately 30% of the energy deposited in the TMP cell.

The TMP cell was located at the focus of the beam and was followed by SV2, another veto scintillator (25.7 cm from the end of the beam pipe) with a 2.54 cm hole in the centre. The two veto counters defined an acceptance region which ensured that the particles would pass through the centre of the metal cell where the edge effects from the applied electric field could be neglected. A 1.2 cm diameter, fully depleted silicon surface barrier detector with a $500 \mu\text{m}$ active layer followed this scintillator. This detector was used to measure the dE/dx of the incident particle with a resolution of $\sigma_E/E = 9\%$ which could then determine the particle's velocity, and thus the particle type. The two scintillators, S1 and S2, were $10 \text{ cm} \times 10 \text{ cm} \times 0.635 \text{ cm}$ plastic scintillators used to determine the time-of-flight (TOF) of the incident particle. They were separated by 3.4 cm and were 35.4 cm from the end of the beam pipe. They were thicker than ST1 and ST2 to ensure that large signals were collected giving a more accurate TOF determination. The final element in the detector telescope was a 12.7 cm diameter \times 12.7 cm thick sodium iodide (NaI) scintillator detector 40.3 cm from the end of the beam pipe. This detector was designed to stop the particles and thus measure

their total energy. The higher momentum pions did not stop, but deposited a significant portion ($\sim 30\%$) of their energy in this detector.

The high voltage for the scintillators and the NaI detector was provided by a Lecroy 4032A power supply while the voltage for the silicon detector and the TMP cell was supplied by two Bertran 380X power supplies. A voltage region of high efficiency was determined for each scintillator, with discrimination thresholds at 100mV, and set as the working voltage.

The trigger for the data acquisition is shown in Fig. 3.6. Pulses from the two upstream scintillators, ST1 and ST2, were set in coincidence with each other and in anti-coincidence with the first veto counter giving an output gate width of 50 ns. The gate defined the timing for the start of the data acquisition and so was delayed to position it inside the gates of the rest of the trigger elements. Similarly, the two downstream scintillators, S1 and S2, were set in coincidence with each other with an output gate width of 70 ns. These two gates were set in coincidence with the NaI detector (63 ns gate) and in anti-coincidence with the second veto counter (200 ns gate) to produce the full trigger.

The scintillators (excluding the veto counters) and the NaI detector were connected to charge integrating analog-to-digital converters (ADC). Each counter was also connected to two scalers. One scaler counted the signals from the counter during the triggered gate of the transient analyzer and the other counted continuously from the end of one gate to the end of the next. This can be used to determine the deadtime of the detector array. The silicon detector was connected to a Tennelec TC170 preamplifier and then to two Ortec Model 474 timing filter amplifiers (TFA's). One of these

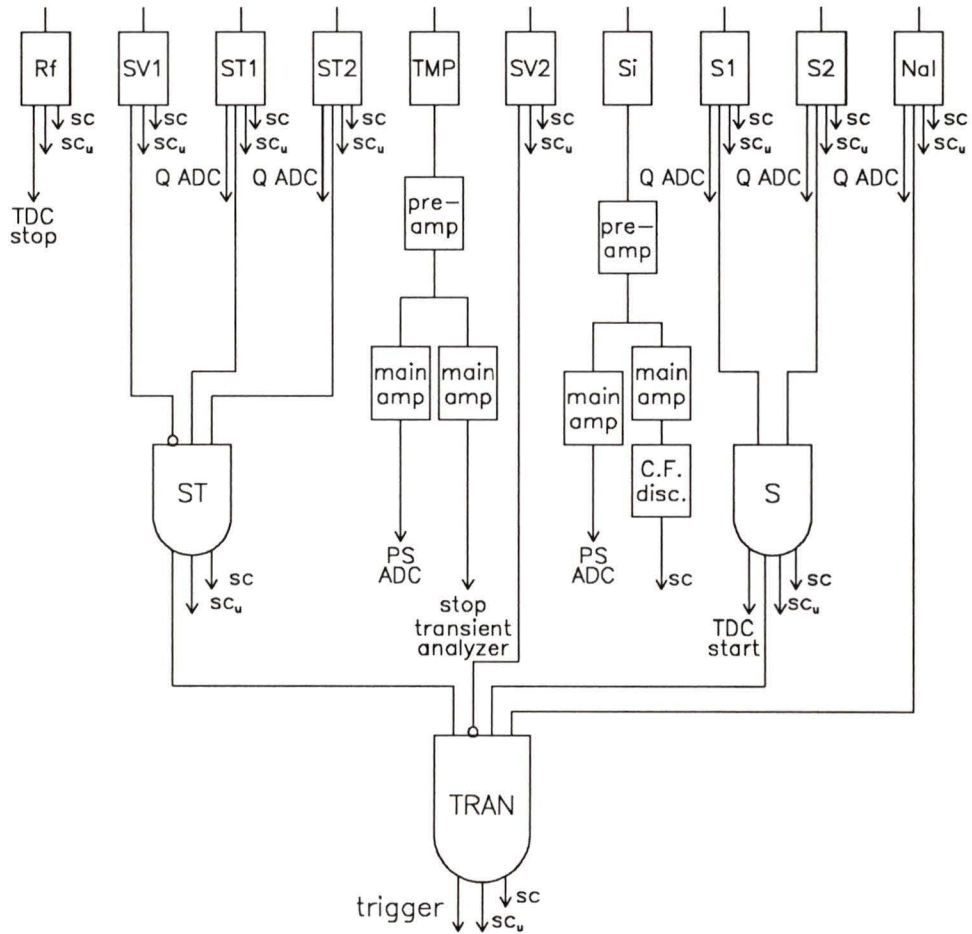


Figure 3.6: Trigger logic and amplifier configuration.

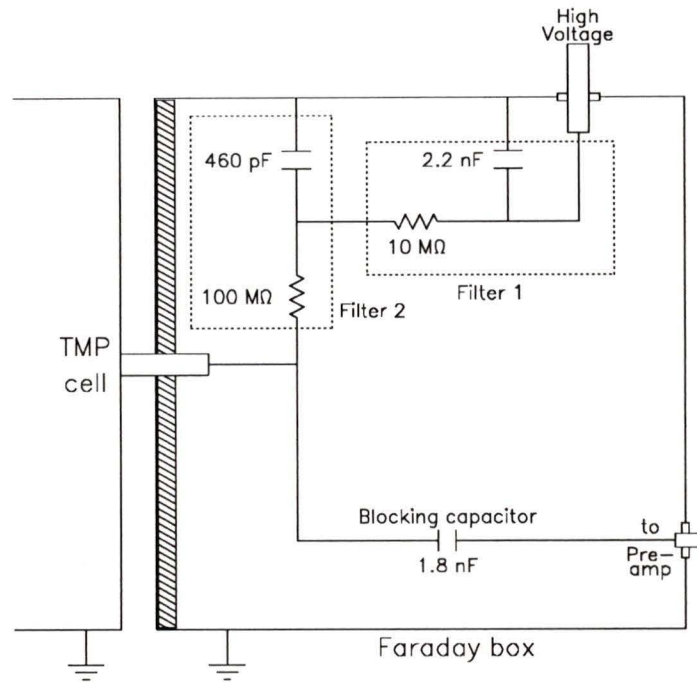


Figure 3.7: Cell electronics.

amplifiers amplified and shaped the signal before passing it to a peak sensing ADC which was used to determine the velocity of the particles by measuring the energy deposition (dE/dx). The other amplifier passed the signal to a constant fraction discriminator which triggered a scaler to count these events. All scalers were reset to zero after each trigger.

3.5 Readout Electronics for the TMP Cell

The high voltage supplied to the cell and the connection to the preamplifier is shown in Fig. 3.7. The Faraday box containing these electronics was designed to prevent any exterior Rf noise from entering and creating electronic noise. A rubber shield was also placed at the front of the box to prevent ‘sparking’

between the grounded box and the high voltage supply to the cell. The high voltage supply was filtered prior to entering the box with a passive low-pass filtering system to remove fluctuations in the voltage due to any external Rf sources and due to fluctuations in the power supply itself. Inside the Faraday box there were two additional low-pass filters to remove any further Rf noise which may have leaked into the box and to remove the effects of any sparking which could have occurred within the box. The second filter also helped to prevent the voltage supply from dropping when a pulse was collected. A blocking capacitor was placed between the electrode feedthrough and the connection to the preamplifier to prevent the high voltage from being placed directly on the preamplifier.

The cell was connected to a Tennelec TC170 preamplifier and then to two TFA's (see Fig. 3.6). These timing filter amplifiers acted as a bandpass filtering system to reduce high and low frequency noise from the signal. Again, one of the TFA's shaped the signal and passed it to a peak-sensing ADC to be used for online signal monitoring and analysis of the peak height distribution. The other TFA had much less shaping and acted as the main amplifier for the signal being passed to a transient analyzer. The transient analyzer digitally recorded each signal at 25 MHz for $245.68 \mu\text{s}$. The full pulse shape provides more information on properties of the liquid (eg. drift time, free electron lifetime, and pulse height) than does the pulse height alone. In addition, a pre-trigger region of $40.96 \mu\text{s}$ was defined in order to obtain a baseline measurement for each pulse which provided an accurate measure of the true peak height on individual pulses. Recording the full shape also allows for off-line digital processing of the signals in order to reduce noise contributions even further.

Particle Type	Beam Momentum (MeV/c)	Cell Voltage (V)
p	400	500
p	400	1000
p	400	1500
p	400	2000
p	400	2500
p	400	3000
π	150	500
π	150	1000
π	150	1500
π	150	2000
π	150	3000
π	400	500
π	400	1000
π	400	1500
π	400	2000
π	400	2500
π	400	3000

Table 3.1: Runs used in analysis.

3.6 Data Collection

For this analysis, the cell was placed perpendicular to the beam and the voltage on the cell was varied between 500 V and 3000 V in 500 V increments. The configurations used are listed in Table 3.1. There was no data taken for the 400 MeV/c π 's at 2500 V. It was felt that these runs sufficiently covered the ranges necessary to investigate the voltage dependence of the Birks factor and the energy loss dependence of the Onsager and Jaffé theories. For each configuration of particle type, momentum, and voltage, about 12000 events were taken with each event containing the full digitized signal from

the transient analyzer as well as the information from the ADC's, the TDC and the scalers. Each event was written to magnetic tape for later off-line analysis.

Several calibrations runs were also performed to provide information on the noise (both acoustic and electronic) and to measure the response of the amplification chain. The response was measured by applying a known step voltage onto a test capacitor which converted the step into a delta function and passed it to the amplification chain. This gave the response of the electronics to a simple input which could then be more easily modelled. The noise measurements were obtained by triggering the data acquisition with no pulses being applied to the amplification chain and recording the output 'signal' from the amplifiers.

During the run, several quantities were monitored. Histograms were recorded from each ADC and from the Rf TDC, and individual pulses could be viewed to ensure that the transient analyzer was recording good signals. The scaler counting rates were monitored giving trigger rates typically between 10 and 50 Hz and data acquisition rates typically around 6 Hz. A set of mechanical jaws located after the septum magnet and a vertical slit at the midplane focus of the M11 channel provided a means of controlling the trigger rates to reduce the possibility of double pulses in the transient signals.

Chapter 4

Data Analysis

A four pass analysis of the data which had been written to the magnetic tapes is made. The first pass performs preliminary compression of the data to make it more computationally manageable. The second pass collects histograms of the pulse height and time-of-flight information from the data tapes and performs preliminary data selection based on these histograms. A digital filter is developed to identify double peaks and to allow for better peak height determination of the individual pulses.

The third pass selects data on the basis of linear fits to the pretrigger region of the pulses to remove some noise contributions. Fits to average pulses from each data set, and to the response function data, are performed to determine the applicability of the selection criteria and to determine the parameters of the models. Theoretical pulses using these parameters are passed through the digital filter to determine the gain corrections for the different electric fields. In the fourth pass, digital filtering of the transient signals is performed and the peak heights provided from the filtered signals are histogrammed.

Calibration and systematics are studied using response function and noise data and the errors on the various model parameters are presented.

4.1 Data Compression

The first pass through the analysis consisted mainly of compressing the data to make it more computationally manageable. The 6142 channels comprising each waveform from the transient analyzer were divided into sections of 10 channels. The heights in the 10 channels in each section were averaged and the resulting 614 values were written onto a second tape. The response function data had a much faster rise than the voltage signal data, requiring that more channels be available for fitting this region. Therefore, a compression factor of 2 was used for this data.

4.2 Kinematic Selection Criteria

In the second pass through the data, the pulse height and time-of-flight data from each event were read from the compressed-data tapes and were histogrammed. It was determined that good particle identification and momentum determination could be achieved by applying selection criteria based on the silicon and NaI pulse height data, and from the Rf time-of-flight data. Typical spectra are shown in Fig. 4.1 along with some representative kinematic selection criteria (data in the hatched areas was rejected). The long tail in the NaI data represents particles that stop in the detector due to large energy loss fluctuations. The double peak in the time-of-flight data represents sub-structure in the beam Rf cycle (3-4 ns).

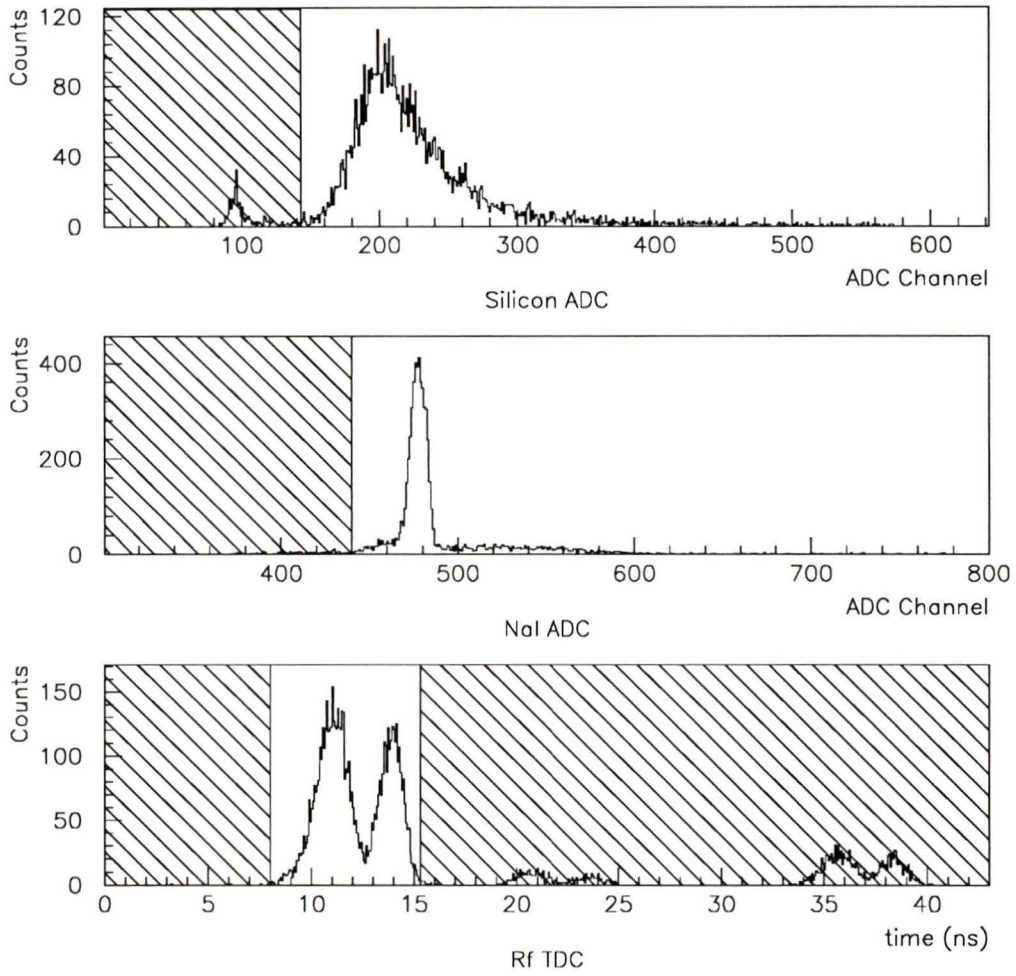


Figure 4.1: Sample of the silicon and NaI pulse height and the Rf time-of-flight spectra. Each spectrum has the other two kinematic criteria already applied.

4.3 Digital Filter Development

Inspection of sample transient waveforms revealed two basic types of corruption of the data: double pulses and low frequency acoustic noise. The double pulses were identified in the data by digitally filtering the transient waveforms and removing events with a poor linear fit in the tail region of the filtered waveform. The digital filter which was developed also selected a narrow frequency band in order to improve the signal to noise ratio on the measurement of the pulse heights (see Appendix B). Two 21 point window filters were used for low pass filtering while a 141 point bandpass differentiator was used for bandpass filtering and for numerical differentiation of the signal. The differentiation of the signal narrowed the pulse used for peak height determination and thus removed double pulse contributions from this result. The combination of the three filters reduced the effects of truncation of the infinite Fourier series representation of the corresponding ideal filters. The final filter was a convolution of these three filters. The frequency spectrum of this filter and the frequency spectrum of the high and low field theoretical current pulses are plotted in Fig. 4.2 showing the frequency region on which the filter would act. Ideally, the filter should act on the region in frequency space where the current pulses start to drop from their maximum values. Note that the abscissa is logarithmic and that consequently, the filter is a narrow spike at relatively low frequency. The minimum width possible for the spike is inversely proportional to the number of terms in the filter. This number is limited by the number of transient channels available. Due to the nature of digital filters, channels at the beginning and the end of each pulse are used for initialization and termination of the filtering procedure.

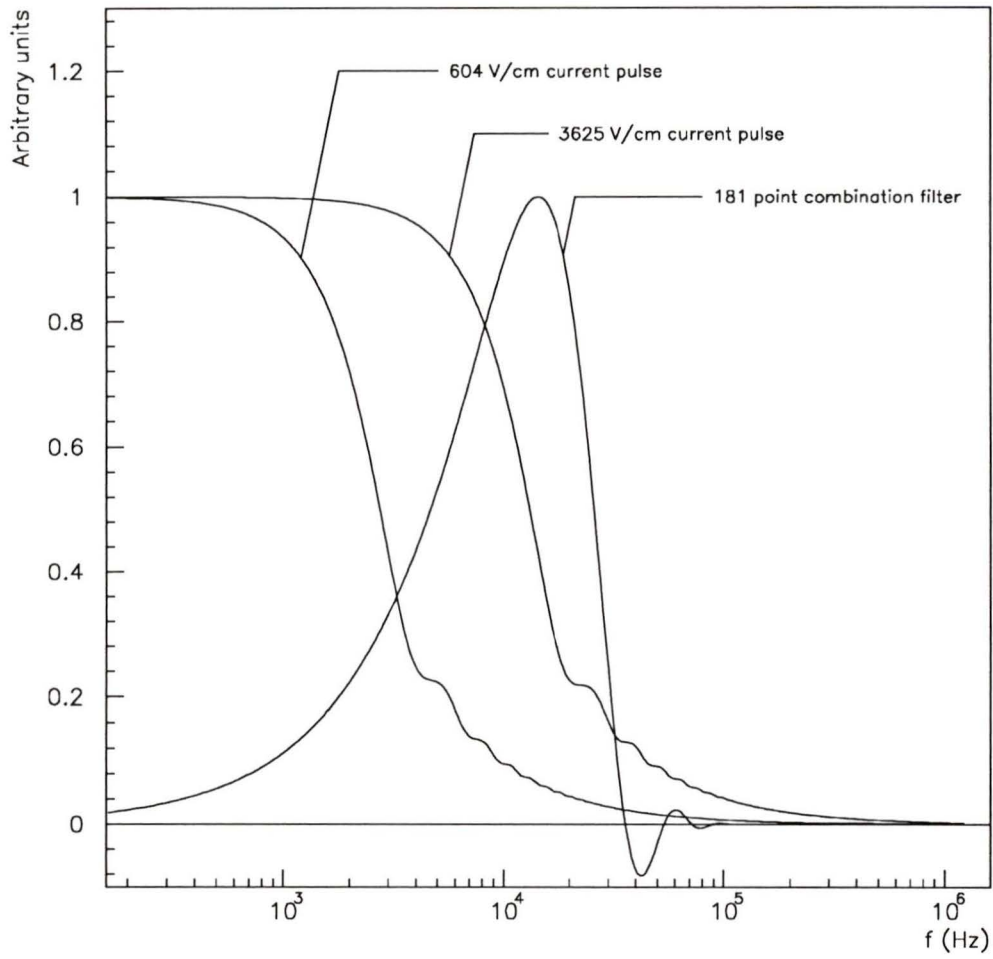


Figure 4.2: Frequency space representation of the low- and high-field current pulses and of the filter.

In order to allow for the initialization, the pretrigger region can be extended by adding several channels with heights determined from a linear fit to this region. Channels must be added until there is a long enough baseline to be able to determine the baseline level of the filtered pulse to subtract for the peak height determination of each pulse. The tail of the pulse could not be extended in this manner without knowing the true shape of the pulse. Thus the filter could not have more than about 1/3 the number of channels in the transient waveform. Figure 4.3 shows the effect of the digital filter on a theoretical pulse.

4.4 Pretrigger Selection Criteria

The third pass applied the kinematic selection criteria and used the digital filter to identify double pulses in the data sets. This pass also removed pulses associated with a high level of low frequency noise by applying further selection criteria which were determined based on an investigation of the pretrigger region of the unfiltered transient waveforms. Since there should be no correlation between the shape of this region and the shape of the pulse, a linear fit to this region, giving values of the slope, the y-intercept, and the sum of the squares of the residuals from this fit (R^2) for each pulse, would provide a measure of the amount of acoustical noise in the pulses. The criteria consisted of rejecting pulses symmetrically on the gaussian histograms of the slope and y-intercept and rejecting pulses with high R^2 .

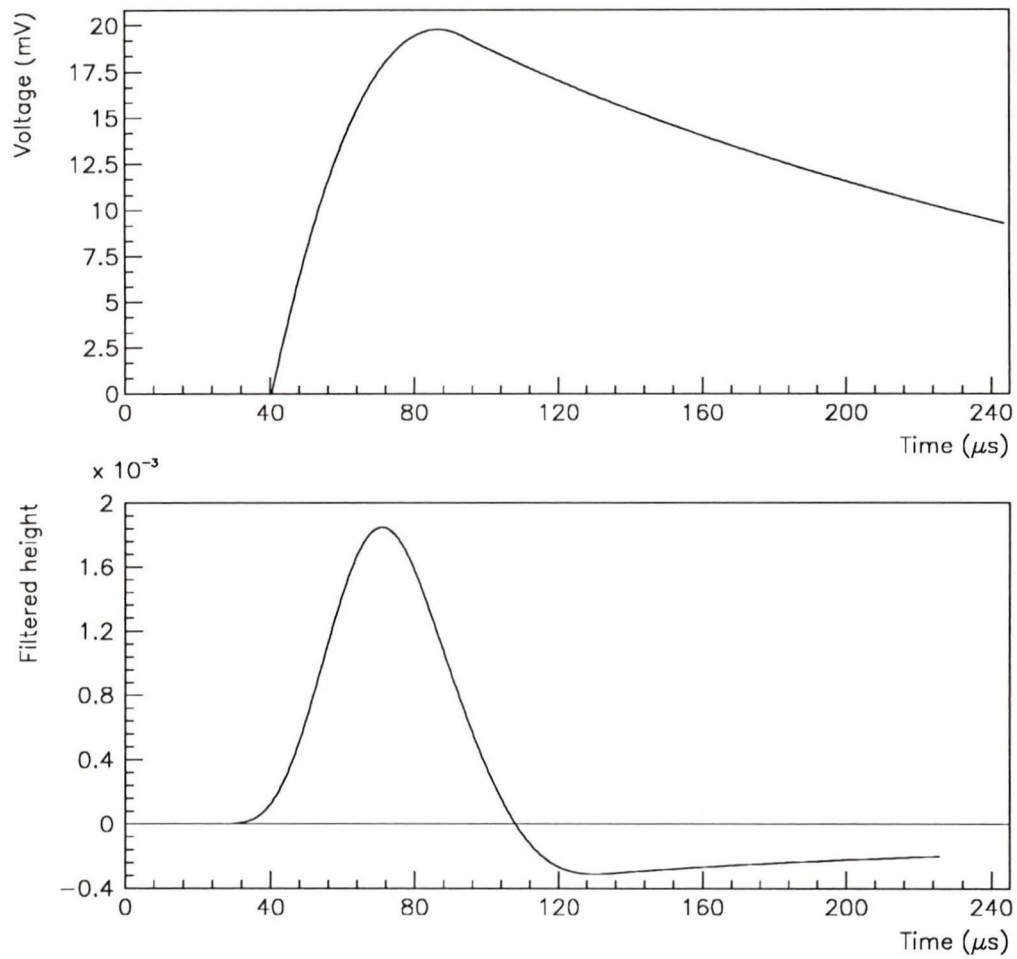


Figure 4.3: (1) A theoretical voltage pulse and (2) the corresponding digitally filtered pulse.

4.4.1 Initial Selection Criteria

To determine initial pretrigger selection criteria, histograms were collected from each data set of the pretrigger parameters from all pulses which were in the valid kinematic regions determined earlier. It was found that some correlation did exist between the pretrigger region parameters and the pulse shape. In a scatter plot of the R^2 against the y-intercept (see Fig. 4.4), a double lobed structure was evident. The average pulses from within these lobe regions are shown in Fig. 4.5. These two regions show a definite trend in the shape of their pulses, and these pulses should be removed from the analysis. Thus the central region was used to determine a preliminary criterion for the y-intercept. Different particle/momentum data sets had slightly different average baseline levels. In order to keep the selection consistent, the window for the y-intercept acceptance had to be shifted between these sets. The width of this window, however, remained constant. Loose criteria were also defined for the slope and R^2 to remove very noisy pulses. These preliminary criteria are shown as the dashed lines in Fig. 4.6.

4.4.2 Optimization of Selection Criteria

The selection criteria were then applied to the 400 MeV/c pion and 400 MeV/c proton voltage data sets and optimized to produce data which could be consistently modelled with Eq. 2.7. For each voltage from these two runs, the average of the pulses passing the kinematic and the pretrigger criteria, as well as an additional criteria to remove double pulses was collected. The double pulse selection was determined by performing a linear fit to the tail region of the filtered pulses and removing those pulses with a high R^2 (see

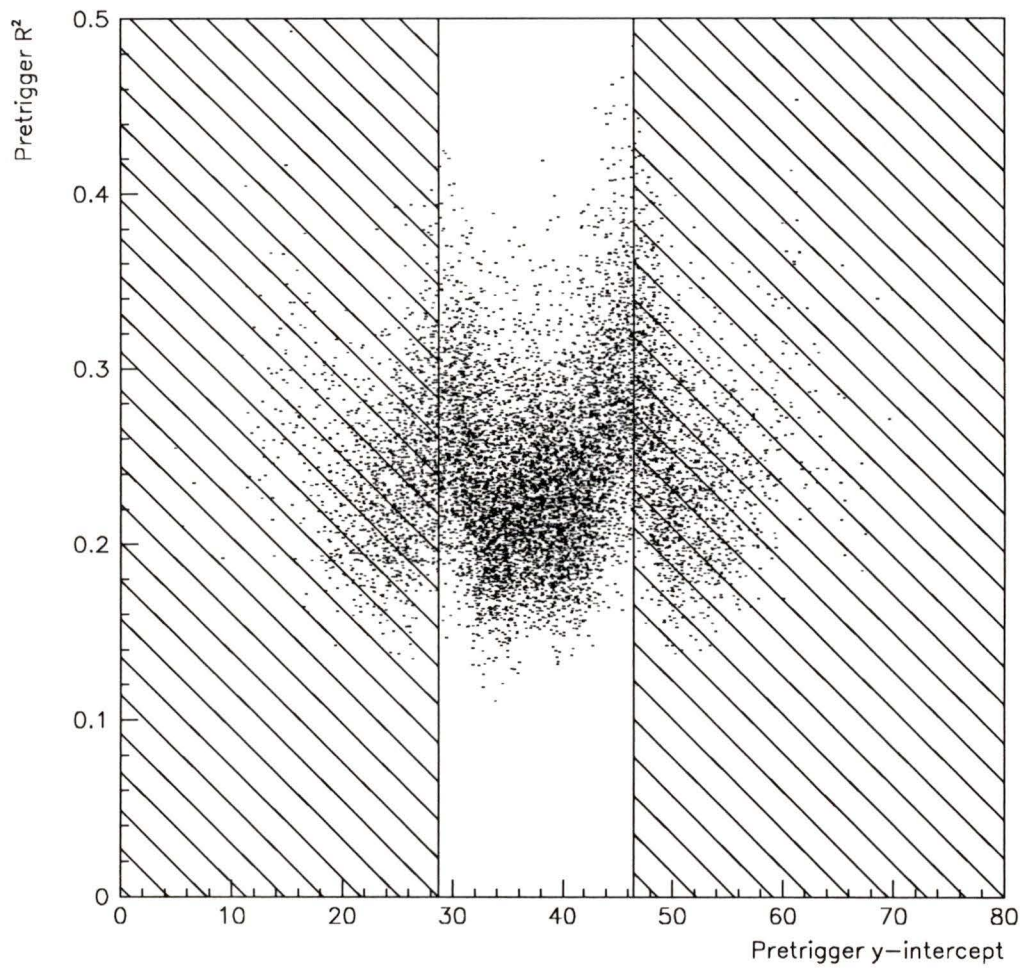
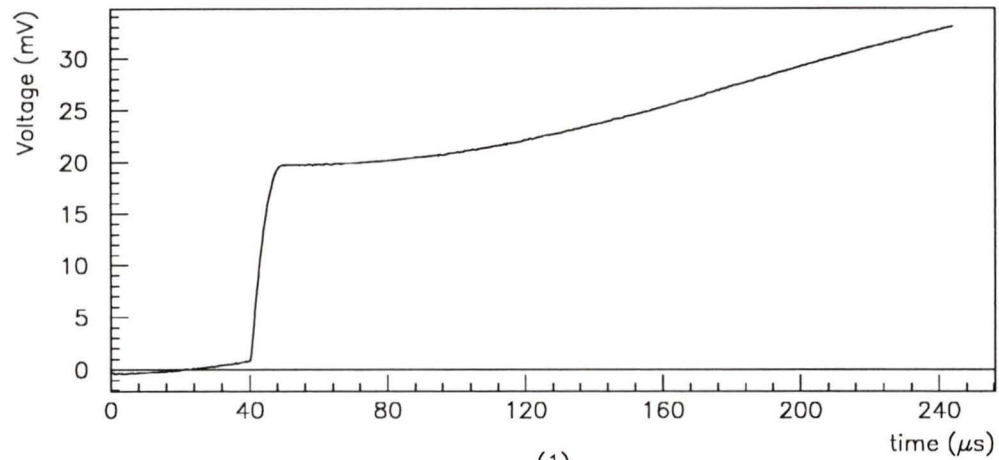
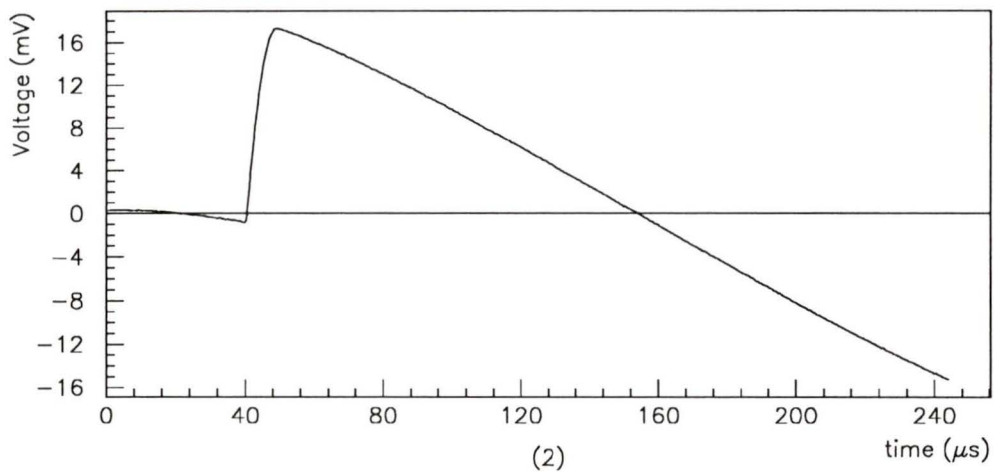


Figure 4.4: Pretrigger scatter plot showing the double lobe structure in the y-intercept data. Events in the hatched regions were rejected.



(1)



(2)

Figure 4.5: (1) shows the average of the pulses with low y-intercept values and (2) shows those with high y-intercept values.

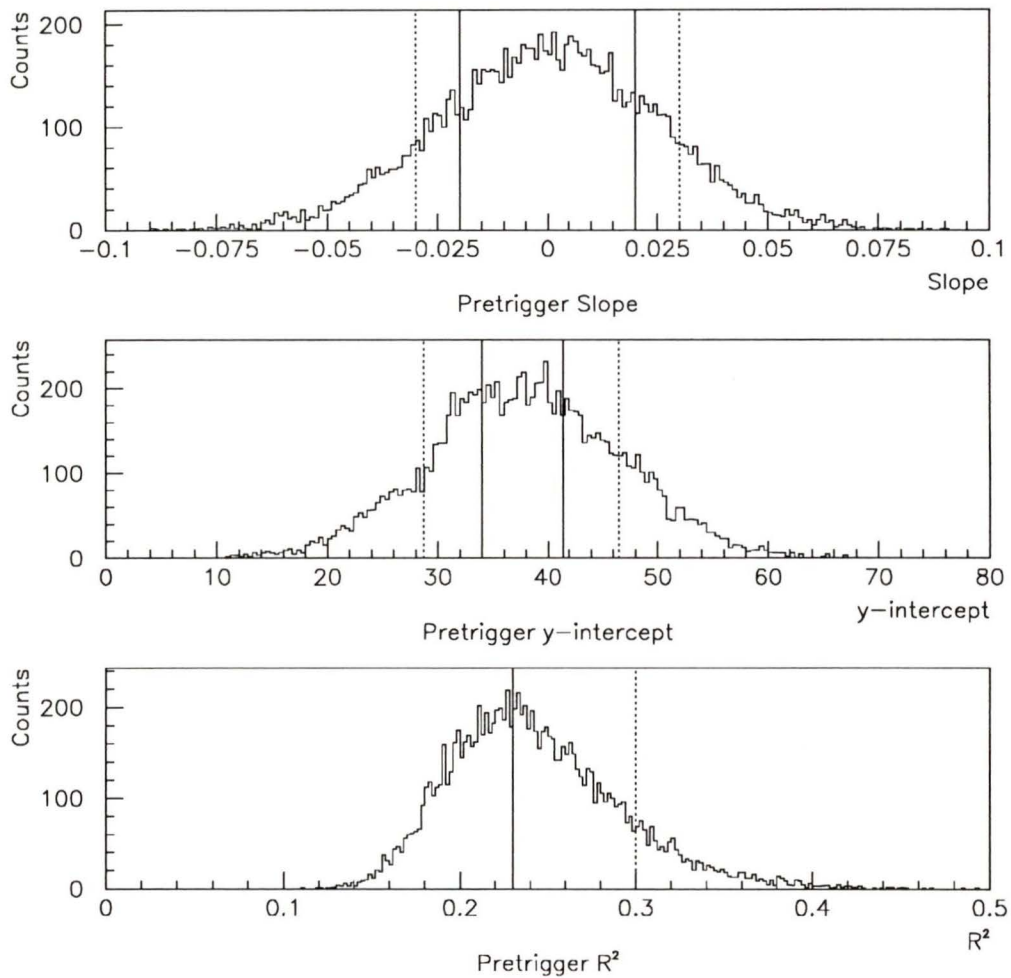


Figure 4.6: Pretrigger selection criteria. The dashed lines represent the preliminary selection criteria and the solid lines represent the final criteria.

Fig. 4.7).

Some of the model parameters in the convolution of the current with the response function (Eq. 2.7) were fixed at values determined by preliminary fits of the response function using Eq. 2.4. An additional exponential term had to be added to this model in order to approximately model some deviations near the peak of the measured response function (see Fig. 4.8). Since the rise of the response function was very short, the integration time constant, τ_1 , was fixed from a preliminary fit at a nominal value of 43 ns. The data was also found to be quite insensitive to the decay time from the preamplifier, τ_2 . Thus this was fixed from a similar preliminary fit at a value of 1.4 ms. This value was consistent with the nominal preamplifier specifications of a decay time between 1 and 1.5 ms. The extra ‘perturbation’ term was also fixed at values determined by fixing τ_1 and τ_2 at the above values, and τ_3 at a nominal value of 285 ns. The perturbation parameters were $A_4 = 0.0604$ and $\tau_4 = 30.541 \mu\text{s}$. The decay time of the main amplifier, τ_3 , was determined by fits to the voltage data sets.

Thus to determine the optimum pretrigger selection criteria, the average pulses from the 400 MeV/c pion and 400 MeV/c proton data sets were simultaneously modelled, allowing τ_3 , μ , τ_ℓ , and the pulse normalizations, Ne , to vary. The sum of the squares of the unweighted residuals per degree of freedom, \tilde{R}^2 , was used to define the quality of the criteria. The preliminary criteria returned a value of $\tilde{R}^2 = 110$. More severe criteria (solid lines in Fig. 4.6) were applied to try to improve the fit and yielded $\tilde{R}^2 = 56.6$. Since even more severe criteria would remove too much data from the peak height

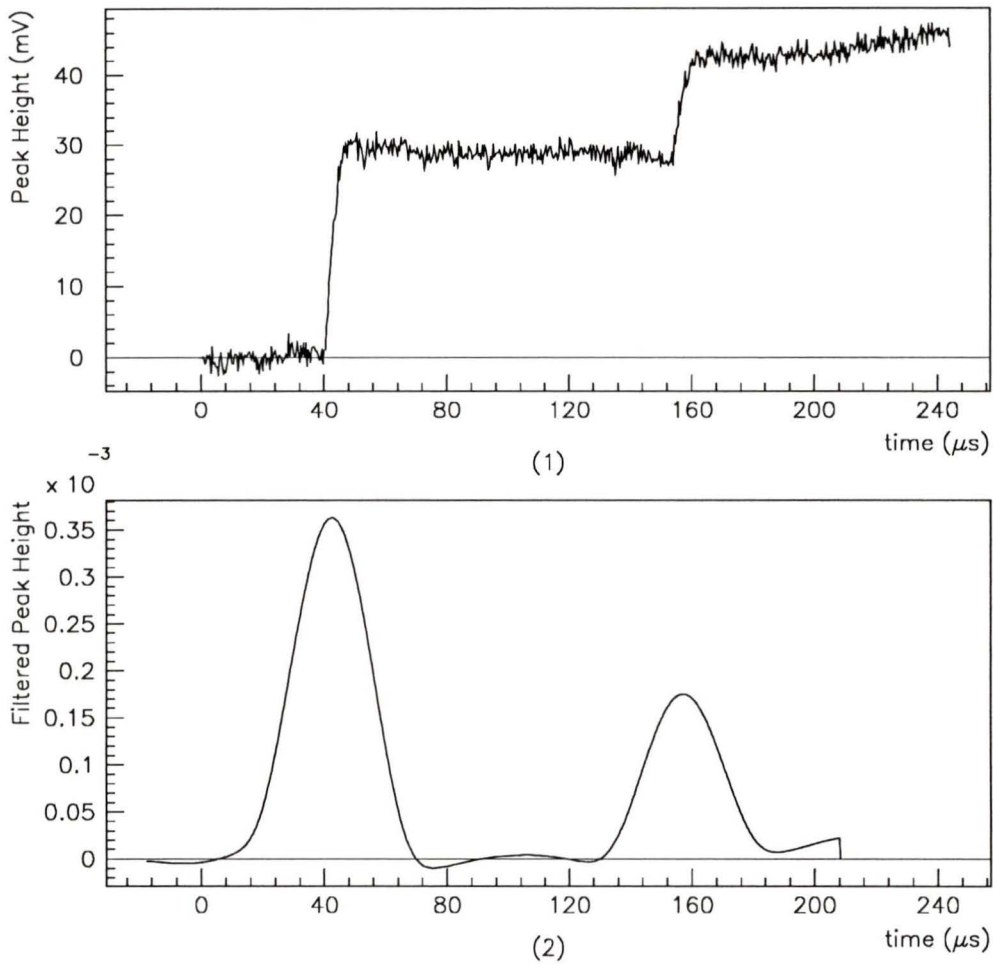


Figure 4.7: Sample of a double pulse. The tail region of the filtered pulse between 80 μs and 200 μs is fit with a straight line and pulses with high R^2 are rejected.

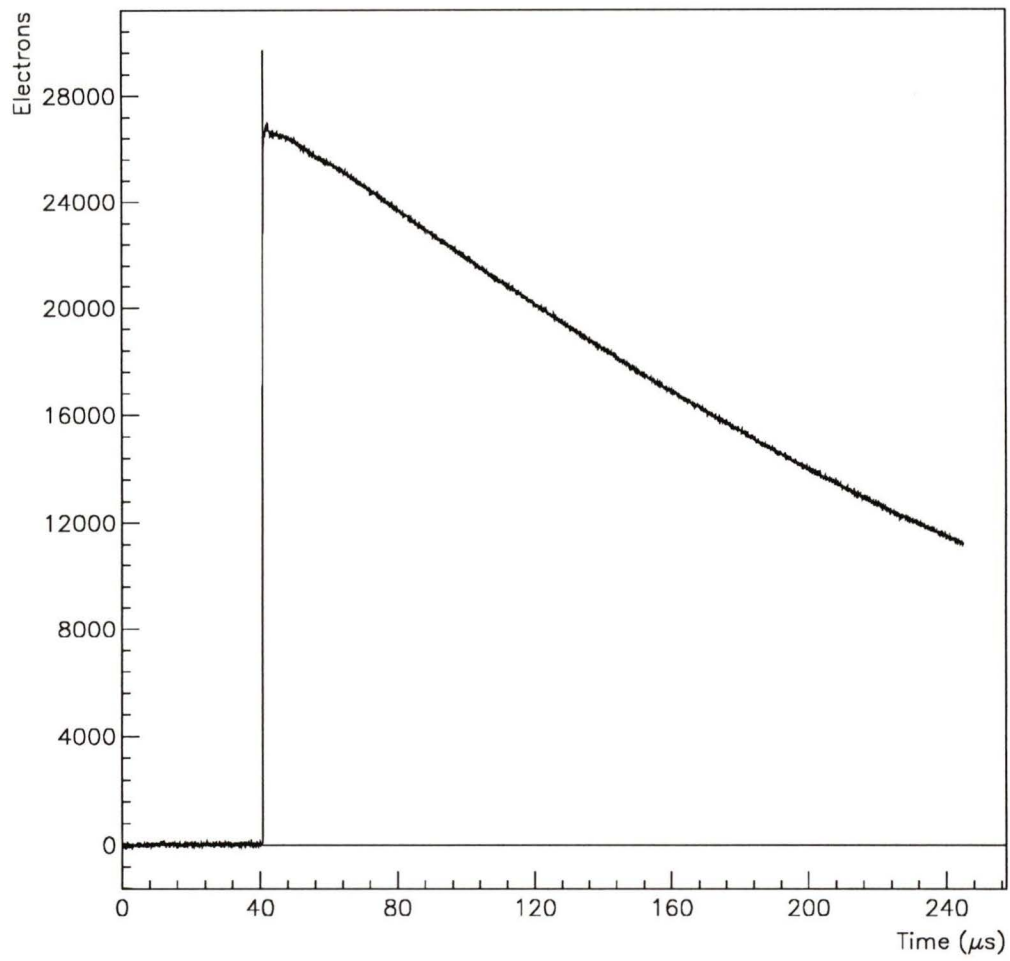


Figure 4.8: Measured response function of the electronics.

distributions, these were defined as the final criteria.

4.5 Final Model Determination

Using these final criteria, the resulting pulse averages from all three particle/momentum data sets were simultaneously modelled, along with the response function with the above parameters fixed at their nominal values, to determine final values of $\tau_3 = 274 \pm 28\mu s$, $\mu = 26.0 \pm 1.9 \text{ cm}^2/Vs$, and $\tau_\ell = 411 \pm 200\mu s$.

The normalizations were also allowed to vary in this fit. The normalization of the response function defines the charge sensitivity of the amplification chain. This determines the conversion factor to calculate the number of electrons collected for each voltage pulse. The input test capacitor which was used for the response function measurement was measured independently as $1.44 \pm 0.14\text{pF}$. If the normalization, N , is given in millivolts, the sensitivity is given by

$$S = \frac{Ne}{C_{\text{Test}} V_{\text{in}}} \quad (4.1)$$

where $V_{\text{in}} = 3.22\text{mV}$ is the input step voltage and $e = 1.602 \times 10^{-19}$ coulombs/electron. The sensitivity was determined to be $S = 1.60 \pm 0.16\mu V/\text{electron}$.

4.5.1 Gain vs. Voltage Correction

The theoretical voltage function determined by the above model parameters was used to determine the gain corrections as a function of voltage for the amplification chain and for the digital filter. A theoretical voltage pulse of

unit height was produced and was passed through the digital filter. The resulting filtered pulse height defined the gain factor which would then be applied to the filtered pulse peak height distributions.

4.6 Final Peak Height Distributions

The final peak height distributions were collected in the following manner. For each pulse which passed all of the final selection criteria, the maximum height of the filtered pulse was determined and the transient channel containing this height was histogrammed. The central value of the resulting gaussian histogram was defined as the peak channel for all pulses in that data set. A horizontal baseline was also determined for each filtered pulse. This was subtracted from the height of the filtered pulse in the peak channel defined above to determine the filtered pulse peak height. The gain corrections were applied to these peak heights to obtain the absolute peak heights in terms of the number of electrons collected. These absolute peak heights were then histogrammed. An example is shown in Fig. 5.1 of the next chapter where these data will be interpreted.

4.7 Errors on the Parameters

The errors on the response function parameters constitute a significant systematic error on the gain corrections and thus on the absolute peak height determination. The systematic error on τ_3 was used to absorb all of the systematic errors in the response function due to any inconsistencies of the fit to the voltage function for each field, and was determined by fitting each average voltage pulse individually, allowing τ_3 and Ne to vary. Due to the

high correlation between τ_3 and Ne_{Test} , the new values of τ_3 were used in separate fits of the response function model to the measured impulse response to determine the effect on the normalization, Ne_{Test} . Theoretical pulses for each voltage were generated with these new values of τ_3 and Ne_{Test} and were passed through the digital filter. The resulting gain corrections using these response function parameters were then compared with the nominal response function gain corrections, with the largest percent deviation being defined as the systematic error in the peak height due to the model. This contributed a 2.7% error to each peak height error independently.

The error on the lifetime was determined by fitting only the low-field data from the 400 MeV/c pions with all parameters except τ_ℓ and Ne fixed. Again, theoretical voltage pulses were determined with the value of $\tau_\ell + \delta\tau_\ell$ and the percent deviations in the gain correction were defined as the systematic error contributions to the peak heights due to the error in τ_ℓ .

The error in mobility was determined by fitting individual voltage data sets with only μ and Ne allowed to vary. The average of the resulting mobilities was calculated and the difference between this result and the nominal result was defined as the error in the mobility. Li [12] has measured the mobility in a similar manner and has obtained consistent results with a smaller error. Due to the large error in the mobility obtained in the present analysis, Li's result of $\mu = 26.3 \pm 0.8 \text{ cm}^2/\text{Vs}$ will be used for the rest of this analysis.

The errors on the lifetime and mobility contributed to the peak height errors in a similar manner. These contributions varied between voltage data sets, but were identical for a given voltage set regardless of the particle type and momentum. Furthermore, for a given voltage, a shift in lifetime or mobility would produce a uniform shift in the peak heights for each particle

type and momentum.

The 10% error in the sensitivity only contributed a 10% error in the level of each peak height. A shift in sensitivity would produce a global uniform shift in peak height for each particle type, momentum, and voltage.

Chapter 5

Results and Discussion

The peak heights are now used to determine the free ion yields. The average energy loss in each element of the detector array is determined using the fits to Janni's tables. This allows for an accurate determination of the energy deposited in the TMP cell. The peak height distributions are then fit with a Vavilov curve which has been convoluted with a gaussian in order to account for any noise contributions which were not removed by the data selection criteria already imposed. The free ion yields are determined from these fits.

The free ion yields are then modelled to the recombination theories discussed earlier. The free ion yield at zero field (G_{fi}^0) for the 400 MeV/c π data is determined in the context of Onsager's theory and compared to Li's results from minimum ionizing cosmic rays. Onsager's theory is then used to determine the free ion yields at zero field (G_{fi}^0) for the other two particle/momentum sets. This theory is also used to determine the Birks factor under the two different assumptions that (1) the Birks factor is voltage independent and (2) the Birks factor is voltage dependent. Finally, Jaffé's columnar recombination theory is used to model the free ion yields.

Particle type	Momentum (MeV/c)	$\langle \Delta E \rangle$ (MeV)
p	400	12.41 ± 0.37
π	150	3.86 ± 0.12
π	400	2.634 ± 0.079

Table 5.1: Average energy deposited in the TMP for each particle/momentum configuration.

5.1 Free Ion Yields

The free ion yield at each voltage and momentum can be determined by converting the peak height distributions into the appropriate yield per energy deposited. The average energy deposited in the TMP for each incident particle type and momentum was calculated from the Chebyshev parameterizations of Janni's tables. The energy lost in each element of the detector telescope was determined and used to find the incident energy on the TMP cell and thus the energy deposited in the cell. The results of this calculation are shown in Table 5.1.

Any noise contributions remaining in the peak height distributions should have a gaussian shape. The peak height distributions were thus modelled with a Vavilov curve convoluted with a gaussian curve. The width of the gaussian would determine the amount of noise in the data and so was allowed to vary in this fit. The free ion yield also varies in this fit and can then be determined from

$$\Delta E = \frac{Ne}{G_{\text{fi}}} \quad (5.1)$$

where Ne is the number of electrons and ΔE is in units of 100 eV. Fig. 5.1 shows a sample of one of the fits. Tables 5.2, 5.3, and 5.4 show the results

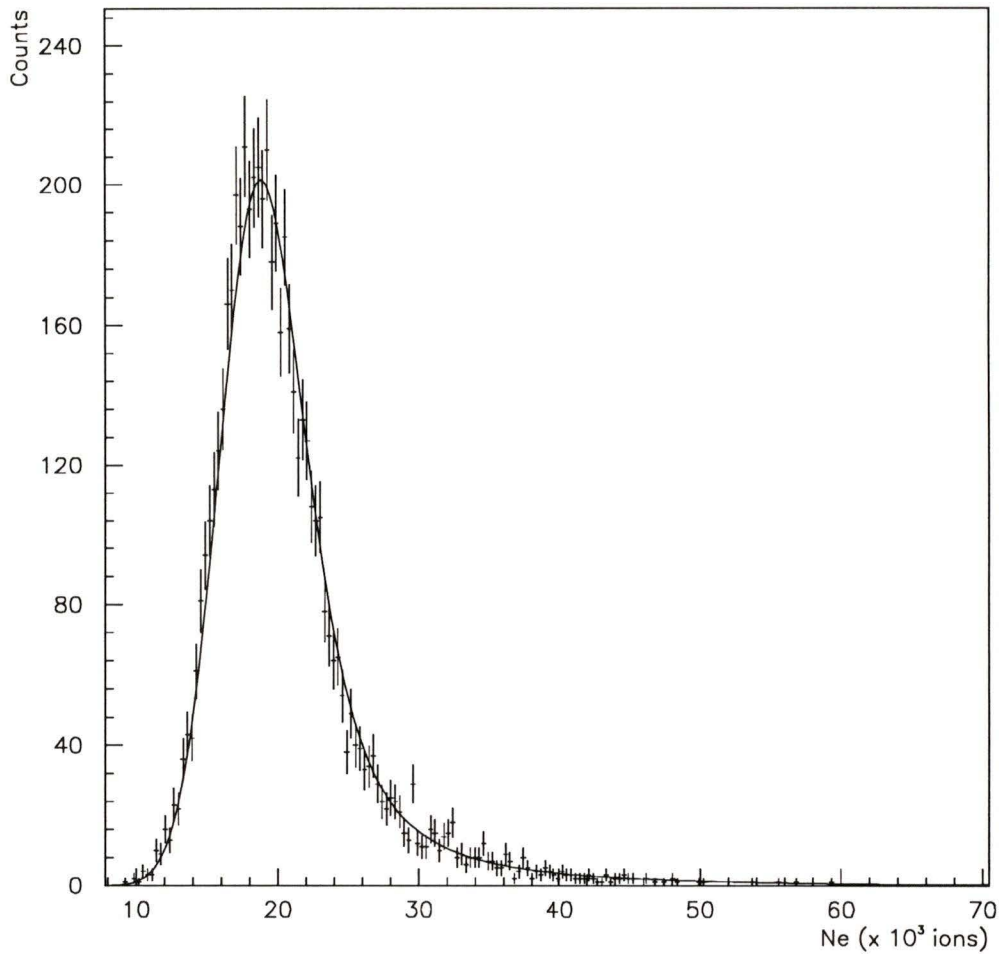


Figure 5.1: Sample fit of Vavilov curve with gaussian broadening for 400 MeV/c pions with an electric field of 604 V/cm on the TMP.

Field (V/cm)	G_{fi} (ions/100 eV)	Fitted σ (electrons)	Number of events in fit
604	0.416 ± 0.011	2807 ± 37	5132
1209	0.445 ± 0.012	2655 ± 39	4220
1813	0.470 ± 0.013	2949 ± 51	3058
2417	0.493 ± 0.013	3216 ± 62	2274
3021	0.511 ± 0.014	3420 ± 83	1806
3625	0.530 ± 0.014	3568 ± 99	1445

Table 5.2: Free ion yields and noise contributions for 400 MeV/c p's.

Field (V/cm)	G_{fi} (ions/100 eV)	Fitted σ (electrons)	Number of events in fit
604	0.732 ± 0.020	2399 ± 74	3175
1209	0.772 ± 0.021	1774 ± 73	2609
1813	0.798 ± 0.021	1739 ± 86	1801
2417	0.814 ± 0.022	1573 ± 209	1439
3625	0.858 ± 0.023	1605 ± 160	727

Table 5.3: Free ion yields and noise contributions for 150 MeV/c π 's.

of these fits to the 17 data sets. The errors in these tables are composed of the statistical error from the fit added in quadrature to the 2.7% error due to the error in τ_3 . The noise data taken during the experiment was used for comparison with the fitted noise. Theoretical pulses of uniform height for each field were added to the noise waveforms and the resulting 'noised' pulses were passed through the filters. The resulting peak height distributions were determined and the widths fitted with a gaussian. These widths ranged from 3578 electrons at 604 V/cm to 1928 electrons at 3625 V/cm. These values are higher than the pion data fitted noise and comparable to the proton data fitted noise widths.

As described in Chapter 2, the initial ion distribution within the cell

Field (V/cm)	G_{fi} (ions/100 eV)	Fitted σ (electrons)	Number of events in fit
604	0.785 ± 0.068	2379 ± 44	5708
1209	0.820 ± 0.022	1676 ± 45	4302
1813	0.848 ± 0.023	1601 ± 54	3235
2417	0.872 ± 0.023	1644 ± 67	2415
3021	0.899 ± 0.024	1574 ± 79	1680
3625	0.913 ± 0.025	1772 ± 108	1241

Table 5.4: Free ion yields and noise contributions for 400 MeV/c π 's.

has so far been assumed to be constant. This is valid for the pions since they are either minimum ionizing or nearly minimum ionizing. The dE/dx for the 400 MeV/c π 's changes by 0.04% over the width of the cell while for the 150 MeV/c π 's, the change is 3%. It is not, however, valid for the protons since the dE/dx changes by 14% over the width of the cell. This large change in energy deposition creates a large non-uniformity in the ion deposition. Since the integrated current from electrons which are further from the positive voltage plate is higher than for those closer to this plate, the non-uniformity will result in a significantly different current contribution from each half of the cell. The combined effect from the two halves, however, will partly cancel each other.

A study was made of this effect in the following manner. The initial ion distribution can be assumed to be given as a function of dE/dx by

$$\lambda(r) = A \frac{dE}{dx}(x) \Big|_{x=R-r} \quad (5.2)$$

where R is the true range of a particle with incident energy E and r is the distance from the grounded plate on the incident beam side of the cell. The

explicit value of A is unknown, but two cases can be compared: (1) where dE/dx is a constant and (2) where it changes over the width of the cell to see what percent change there will be in the calculated ion yield. The total charge collected is calculated as

$$q = \int_0^{t_d} \int_0^{d(1-t/t_d)} \lambda(x) e^{-t/\tau_e} dx dt. \quad (5.3)$$

The constant dE/dx case can be computed analytically, but the changing dE/dx case must be numerically integrated. A 32 point gaussian quadrature algorithm was employed and tested on the constant case to confirm the accuracy of the method. The difference between the two cases amounts to only 0.04%. This small change can be explained by the fact that while the energy deposition is indeed changing, it is almost linear (see Fig. 5.2), and the cancellation provided by the double cell geometry is more complete. The current theory presented in Appendix A essentially reduces the problem of an ionization track to that of a single particle containing all of the charge at some location within each half of the cell. There will be a significant difference in this location between the constant and changing dE/dx cases for a given half of the cell. Due to the near-linearity of the change in dE/dx , however, the effect of this difference will tend to cancel out when both halves are included.

5.2 Onsager Fits

These free ion yields could now be analyzed in terms of the recombination theories discussed earlier. The free ion yield at zero field, G_{f}^0 , was determined

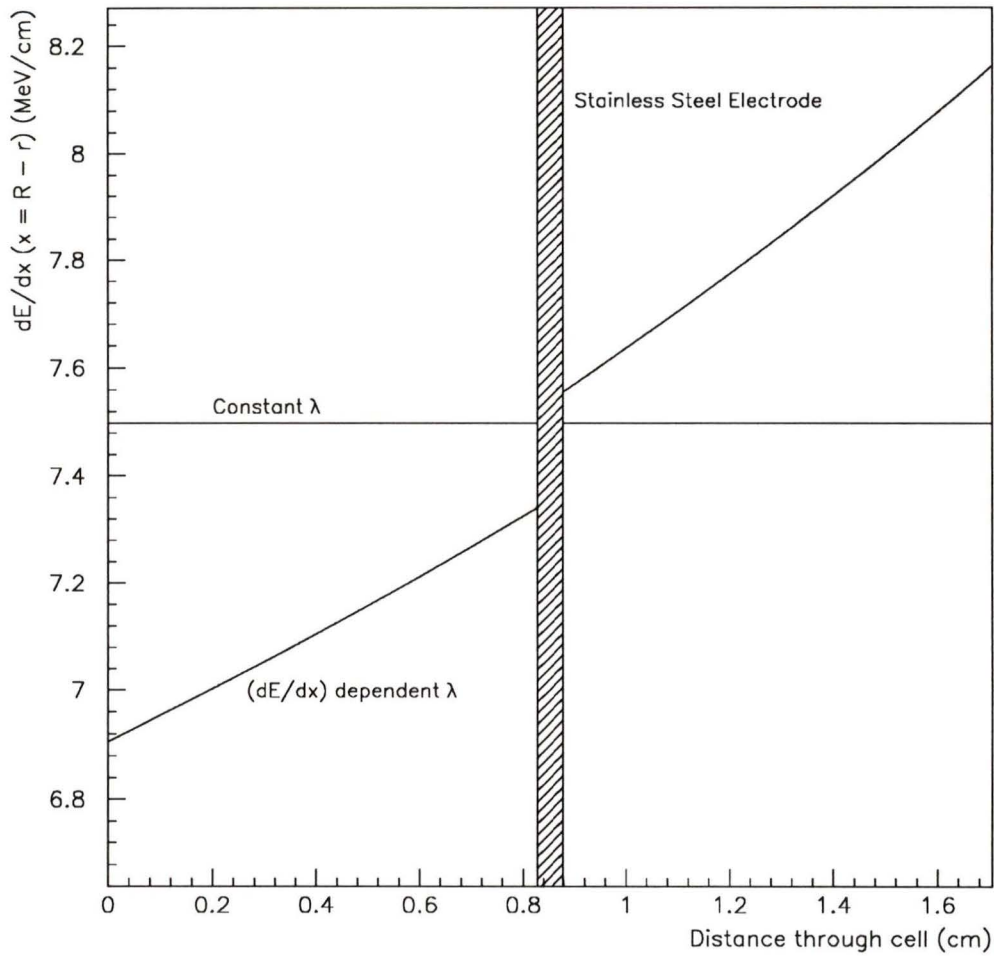


Figure 5.2: Ionization densities for constant and changing dE/dx cases. The gap in the center represents the 500 μm stainless steel electrode which also changes the dE/dx .

Data set	dE/dx (MeV/cm)	G_{fi}^0 (ions/100 eV)
400 MeV/c p	7.49 ± 0.22	$0.426 \pm 0.005(\text{stat}) \pm 0.043(\text{sys})$
150 MeV/c π	2.331 ± 0.070	$0.718 \pm 0.009(\text{stat}) \pm 0.072(\text{sys})$
400 MeV/c π	1.591 ± 0.048	$0.768 \pm 0.009(\text{stat}) \pm 0.077(\text{sys})$

Table 5.5: Zero free ion yields for the three data sets studied.

by fitting the free ion yields with an Onsager model. Each energy deposition, dE/dx , would have a different G_{fi}^0 associated with it and would be modelled by

$$G_{\text{fi}} = G_{\text{fi}}^0 f(E) \quad (5.4)$$

with $f(E)$ given by the right hand side of Eq. 2.18. Fig. 5.3 shows the results of this fit. The results are summarized in Table 5.5. The systematic errors arise primarily from the 10% uncertainty in the charge sensitivity.

Onsager's theory obviously fits the pion data quite well, but has some problems with the proton data. Even so, Onsager's formulation can be used to try to fit the data and find a Birks factor for TMP. If the Birks factor is constant over the range of voltages studied here, the G_{fi} 's can be modelled with Eq. 2.21,

$$G_{\text{fi}} = \frac{A}{1 + kB(dE/dx)} f(E). \quad (5.5)$$

This fit gives $A = 1.000 \pm 0.035$ ions/100 eV, and $kB = 0.178 \pm 0.014$ cm/MeV and is shown in Fig. 5.4. An independent determination of the Birks factor can be performed, without any assumptions about the voltage dependence, by computing the ratios of pairs of free ion yields at each field. Taking the ratio of Eq. 2.20 for each pion data set with the proton data set and defining

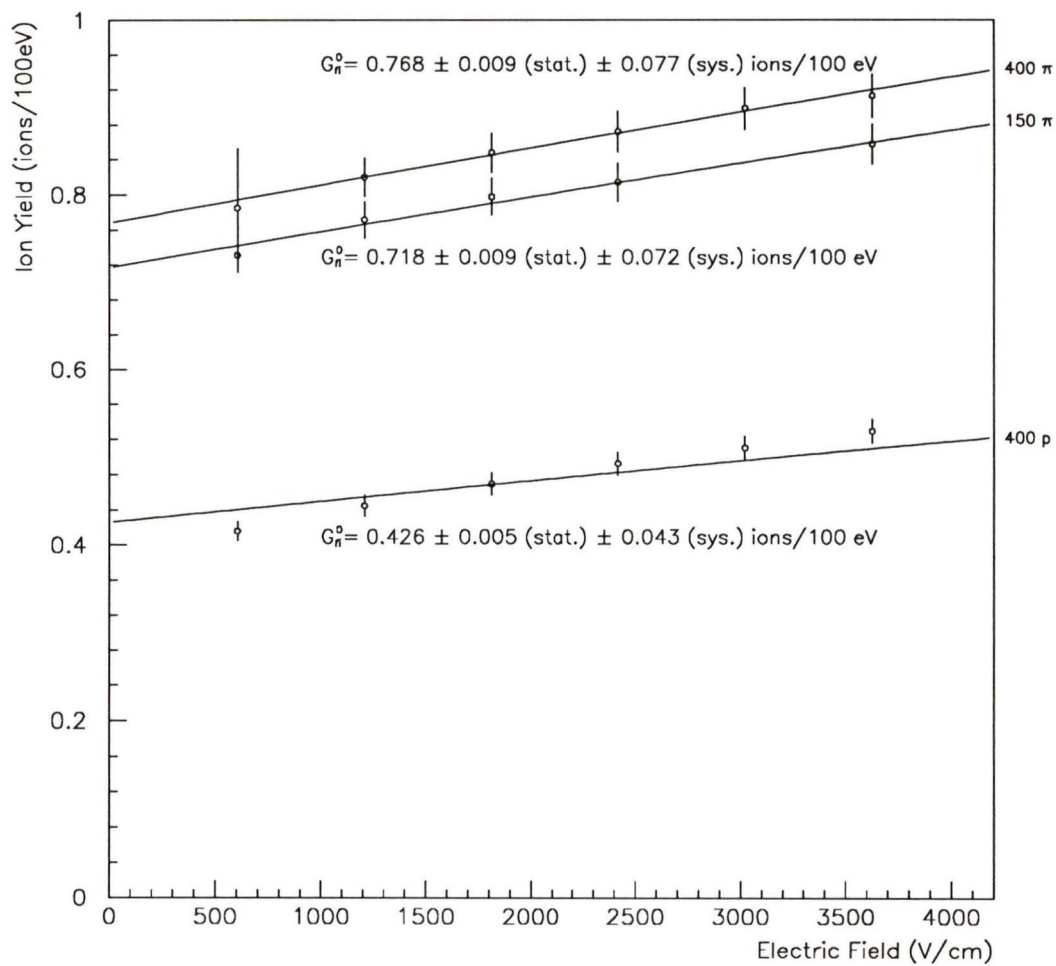


Figure 5.3: Fits of G_{fi}^0 for all data sets.

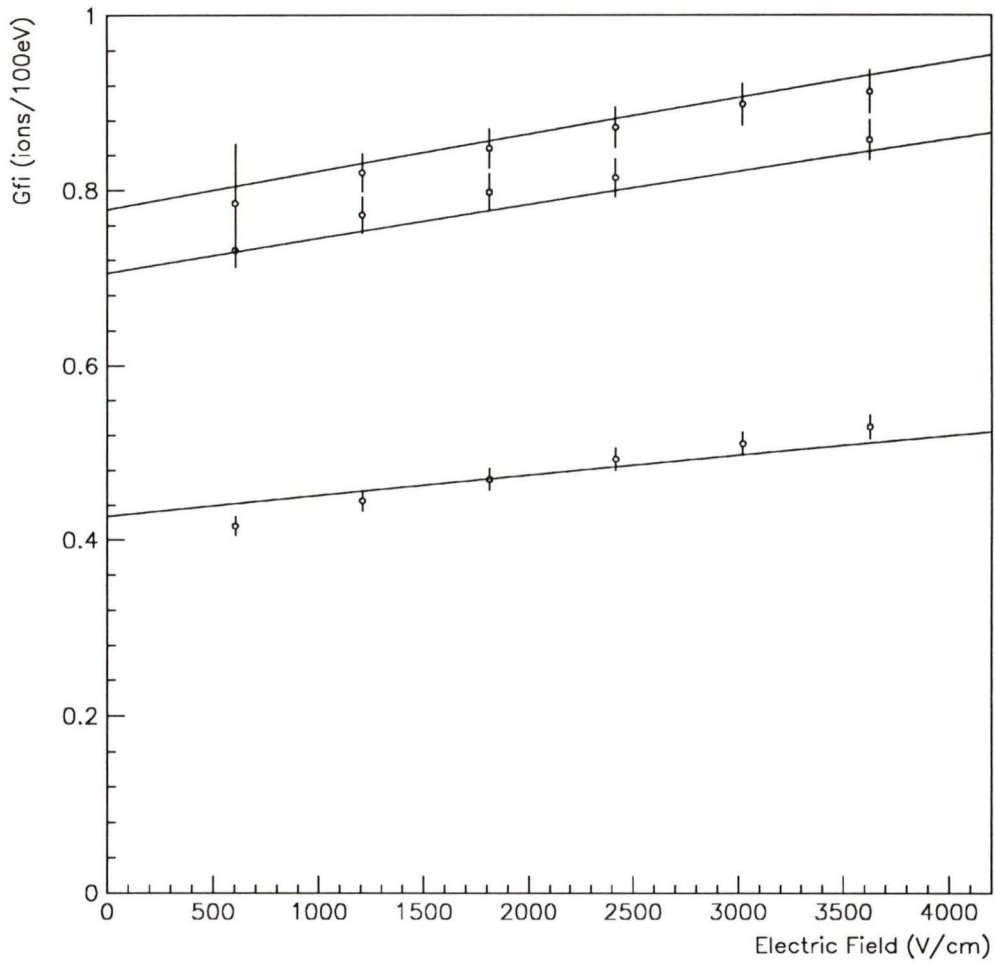


Figure 5.4: Voltage independent Birks factor fit.

Field (V/cm)	Birks factor (cm/MeV)		
	From 400 MeV/c π	From 150 MeV/c π	Weighted average
604	0.197 ± 0.055	0.223 ± 0.040	0.215 ± 0.032
1208	0.185 ± 0.029	0.213 ± 0.038	0.195 ± 0.023
1812	0.174 ± 0.028	0.198 ± 0.036	0.183 ± 0.022
2416	0.164 ± 0.026	0.179 ± 0.033	0.170 ± 0.021
3021	0.162 ± 0.026		0.162 ± 0.026
3625	0.152 ± 0.025	0.166 ± 0.031	0.157 ± 0.019

Table 5.6: Voltage dependent Birks factors.

$G_{\text{fi}} = (dI/dx)/(dE/dx)$, the Birks factor is obtained in the form

$$kB = \frac{G_{\text{fi}}^{\pi} - G_{\text{fi}}^p}{G_{\text{fi}}^p (dE/dx)^p - G_{\text{fi}}^{\pi} (dE/dx)^{\pi}}. \quad (5.6)$$

A comparison of the two pion data sets would have very large errors on the results due to the similarity in dE/dx for the two sets, and so would not give any significant new information. Table 5.6 presents the Birks factor values for the comparison of the two pion data sets with the proton data set and their weighted averages. The weighted averages are plotted in Fig. 5.5 along with the data from Aubert, et. al. [13] for comparison. There is an apparent systematic difference between the two pion data set results which can primarily be attributed to a 3% error on dE/dx . The horizontal line in the figure shows the level of the voltage independent fit for comparison, and can be shown to be the weighted average of the voltage dependent Birks factor values.

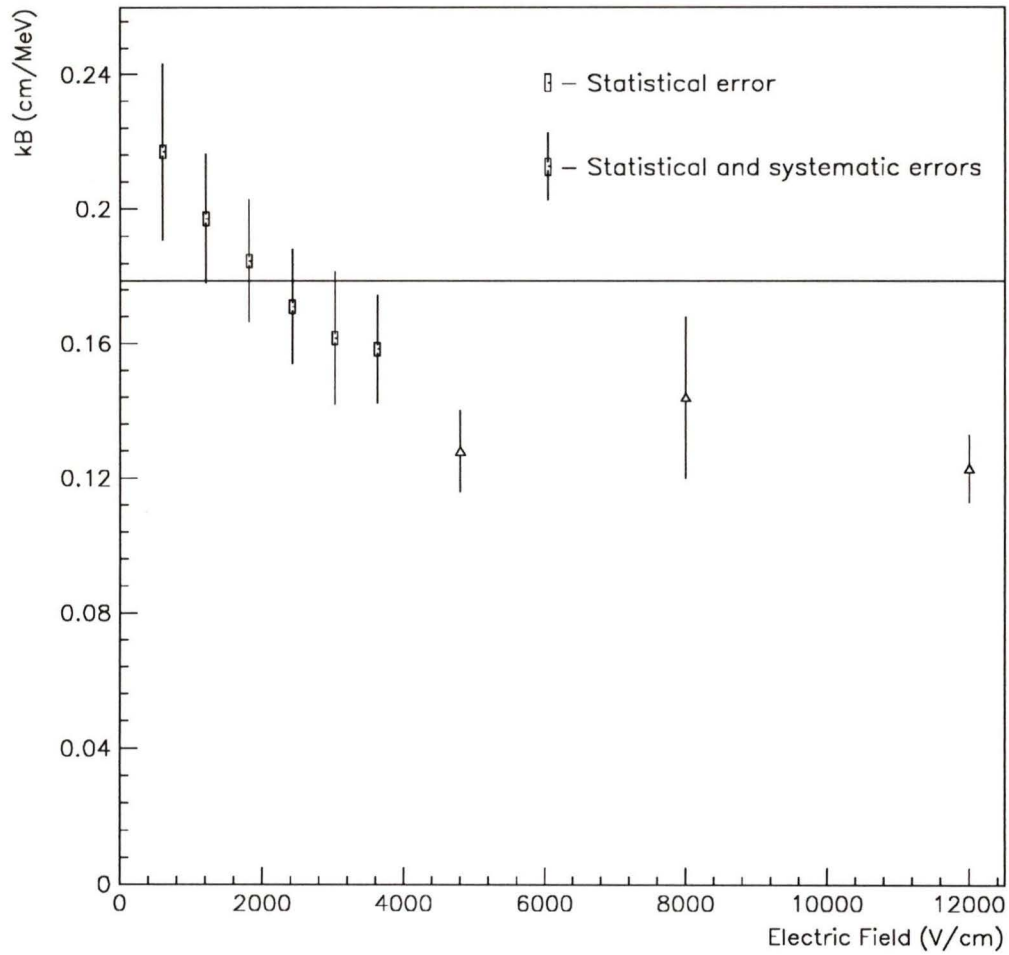


Figure 5.5: Voltage dependent Birks factors. The line represents the voltage independent level. The triangular points represent Aubert, et. al.'s data at $\theta = 0^\circ$.

Contributor	Contribution (%)
$(dE/dx)_{400MeV/cp}$	3.9
$(dE/dx)_{150MeV/c\pi}$	2.2
$(dE/dx)_{400MeV/c\pi}$	4.7
τ_ℓ	0.7
μ	0.5
Statistical and Systematic	4.3
Total	7.9

Table 5.7: Birks factor error contributions.

5.3 Error Contributions to the Birks Factor

The error in the mobility contributed 1.8% to the error in the gain correction at the lowest field and less at the higher fields. This error corresponds to a 0.4% error in the zero free ion yield (see Fig. 5.6) and a 0.5% error in the Birks factor. The lifetime had a more significant contribution to the error in the zero free ion yield as shown in Fig. 5.7. The lifetime contributed a systematic error of 3.3% to the gain correction at the lowest field, and again a lower contribution at the higher fields. This corresponds to a 1.3% error in the free ion yield and a 0.7% error in the Birks factor.

The 3% error on dE/dx gave the largest contribution to all Birks factor fits. This contribution to the voltage independent Birks factor was determined by changing the values of dE/dx for the three data sets independently and fitting a new value of the Birks factor. The differences were then added in quadrature, along with the contributions from the lifetime and mobility errors, to determine the overall error. The percentage contributions are summarized in Table 5.7.

The errors on the voltage dependent Birks factors were computed explic-

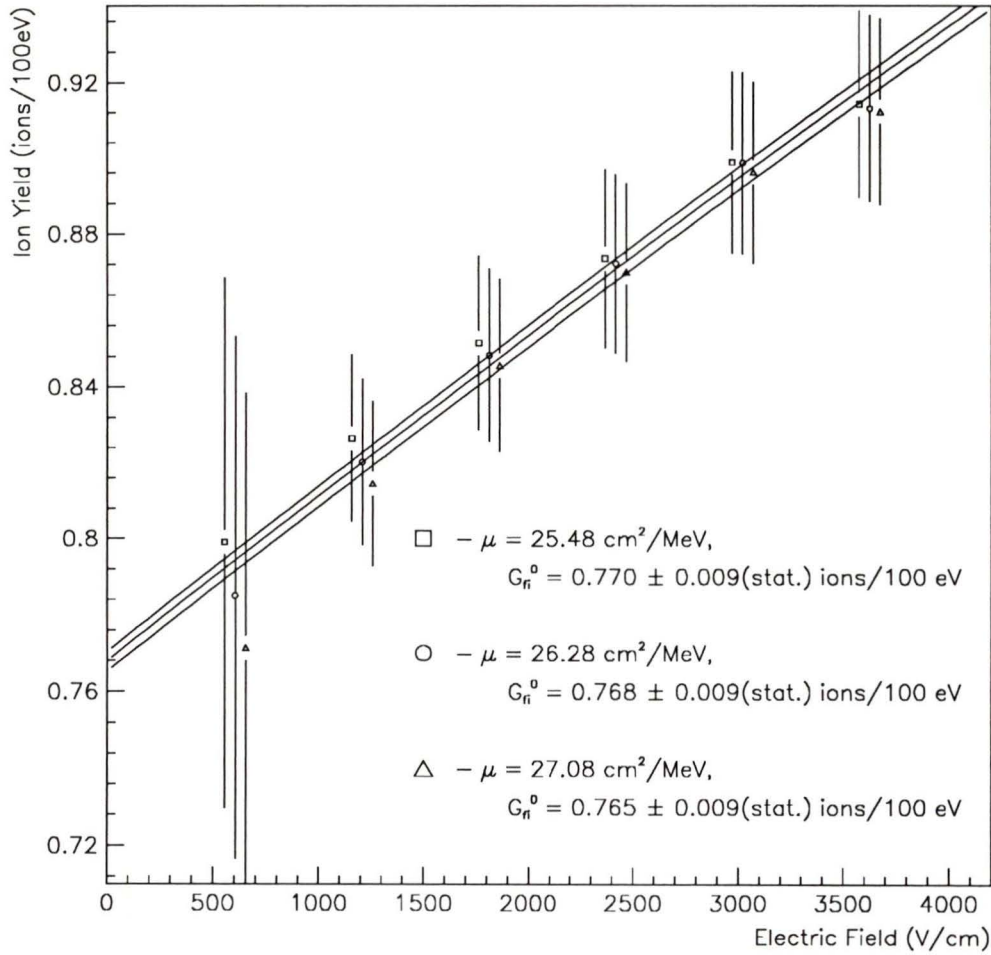


Figure 5.6: Plot of ion yields at limits of μ for 400 MeV/c π data.

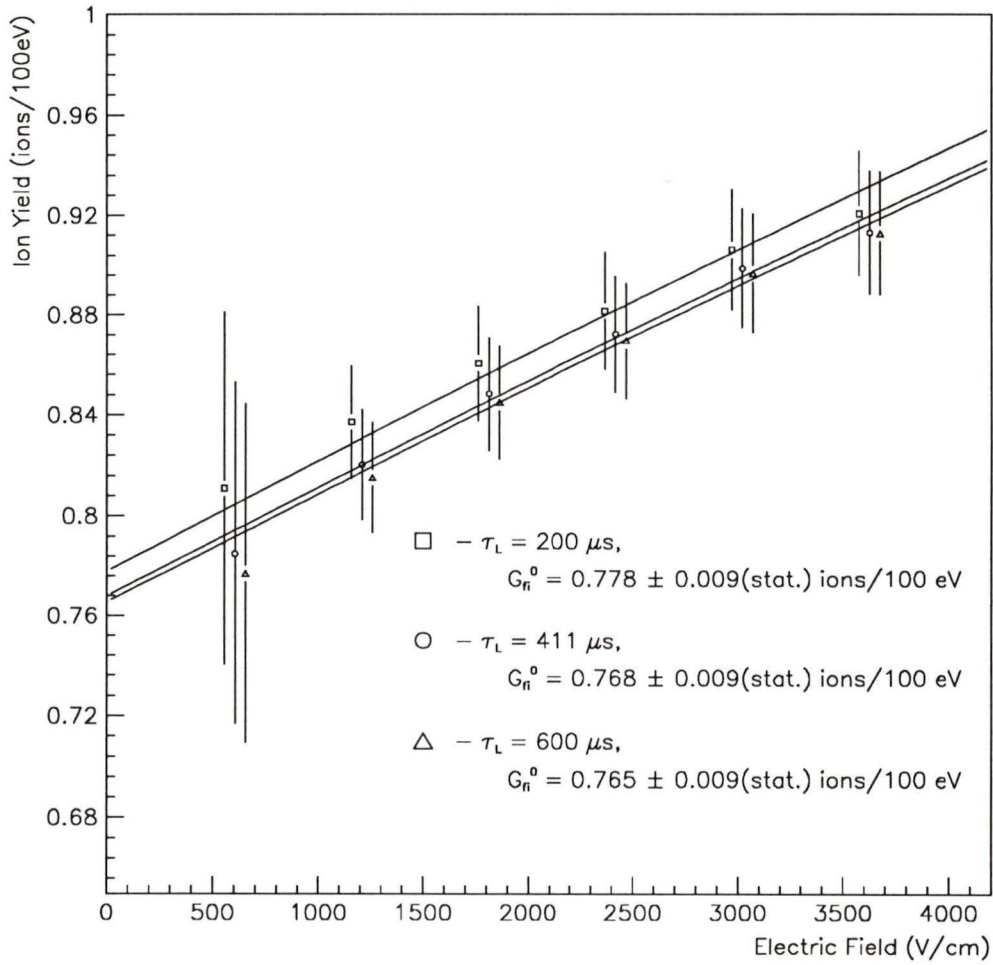


Figure 5.7: Plot of ion yields at limits of τ_ℓ for 400 MeV/c π data.

itly by propagating the errors through Eq. 5.6, resulting in

$$\delta kB = \left\{ \left(\frac{\partial kB}{\partial G_{\text{fi}}^p} \right)^2 (\delta G_{\text{fi}}^p)^2 + \left(\frac{\partial kB}{\partial \left(\frac{dE}{dx} \right)^p} \right)^2 \left(\delta \left(\frac{dE}{dx} \right)^p \right)^2 + \right. \\ \left. \left(\frac{\partial kB}{\partial G_{\text{fi}}^\pi} \right)^2 (\delta G_{\text{fi}}^\pi)^2 + \left(\frac{\partial kB}{\partial \left(\frac{dE}{dx} \right)^\pi} \right)^2 \left(\delta \left(\frac{dE}{dx} \right)^\pi \right)^2 + (\delta kB_\mu)^2 + (\delta kB_{\tau_\ell})^2 \right\}^{1/2} \quad (5.7)$$

where δG_{fi}^π and δG_{fi}^p are the statistical and systematic errors from the pion and proton data set fits, $\delta(dE/dx)^p$ and $\delta(dE/dx)^\pi$ are the 3% errors on the energy depositions, and δkB_μ and δkB_{τ_ℓ} are the systematic error contributions from the mobility and lifetime.

5.4 Jaffé Fits

The final theory investigated was Jaffé's columnar recombination theory. Some slight modifications to the basic theory have been suggested by Muñoz, et.al. [14], involving a constant term which should be added to account for ions which could escape by mechanisms other than diffusion. This term turned out to be significant only in the fit of the proton data set. The three parameters in Eq. 2.27 to be fit were the dispersion parameter (b), the initial ion density (N_0), and the additional constant term (N_{J0}). The fits displayed some anomalous behaviour when all parameters were allowed to vary. The pion data sets fit well giving $b = 581 \pm 490 \text{ \AA}$ which is within error of the value of 390 \AA obtained by Muñoz's group. The large error, however, indicates the severe problems with the application of the theory. This group notes, however, that their result seems rather high, and attribute this to the fact that the electric field in the theory is only the external applied field and does not

Data set	N_0 (Onsager) (ions/cm)	N_0 (Jaffé) (ions/cm)
400 MeV/c p	163855 ± 1923	296568
150 MeV/c π	85851 ± 1076	61913 ± 2470
400 MeV/c π	62699 ± 735	28333 ± 689

Table 5.8: Comparison of total ion yields per centimeter for Onsager and Jaffé formalism. Errors are statistical errors only.

include any electric field components set up by the separation of the positive and negative ions.

The N_{J_0} term for the pion data sets fit to zero while for the proton data set it was 11007 ± 385 ions/cm. The N_0 term produced for the two pion data sets were $N_0^{400\pi} = 28333 \pm 689$ ions/cm and $N_0^{150\pi} = 61913 \pm 2470$ ions/cm. The initial ion density for the proton data set did not converge. The main problem appeared to be that the free ion yield was approximately twice as high as Jaffé's theory predicted for the calculated energy deposition. Eventually, this term was fixed at $N_0^{400p} = 296568$ ions/cm by equating the ratios

$$\frac{N_0^{400p} - N_0^{400\pi}}{(dE/dx)^{400p} - (dE/dx)^{400\pi}} = \frac{N_0^{150\pi} - N_0^{400\pi}}{(dE/dx)^{150\pi} - (dE/dx)^{400\pi}} \quad (5.8)$$

The resulting fit is shown in Fig. 5.8. Using the relation between G_{fi}^0 and G_{tot} (Eq. 2.17), and since $N_0 = 10^4 G_{tot} dE/dx$, where the factor of 10^4 accounts for the definition of G_{tot} in units of ions/100 eV, these results can be compared with those from Onsager's theory. The results are shown in Table 5.8. There does not appear to be any significant correlation between the results given by the two models.

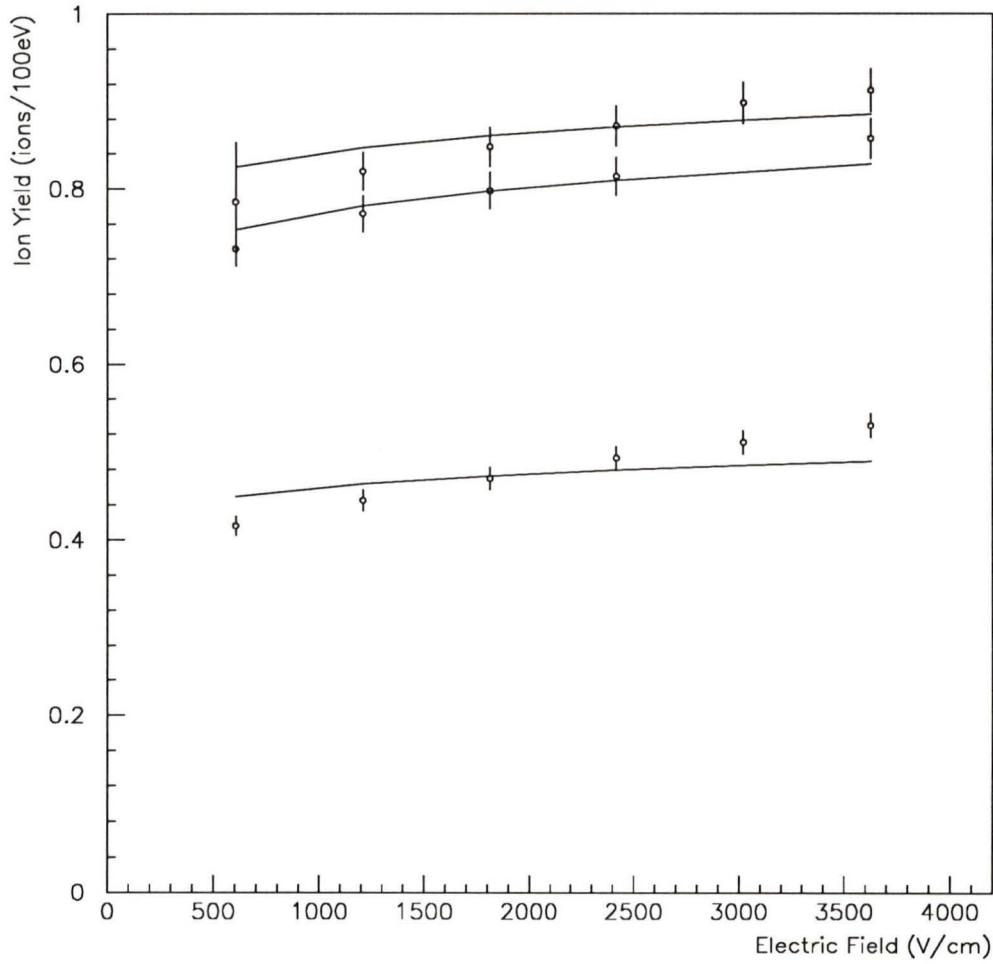


Figure 5.8: Fit of free ion yields to Jaffé's ion recombination model.

5.5 Discussion of the Results

The digital filtering of the voltage waveforms proved to be successful in providing good quality pulses for the analysis. It effectively identified double pulses, supplying more consistent average voltage pulses to be modelled, and providing a measurement of the lifetime and the mobility of the liquid. The low frequency noise in the pulses was also successfully reduced by digitally filtering the waveforms, giving clean peak height distributions and good free ion yield determinations.

Two recombination theories have been used to model the free ion yields: Jaffé's columnar recombination theory and Onsager's initial recombination theory. Onsager's theory has proven to be more successful at modelling the data. The pion data sets were fit very well using this model, but the proton data set showed some systematic differences from the theory. These differences appeared to indicate that there may be some additional voltage dependence in the recombination for higher ionization densities.

This voltage dependence shows up more strongly in the Birks factor determination. Two assumptions were investigated with respect to the Birks factor of TMP: a voltage independent and a voltage dependent Birks factor. The measured voltage independent Birks factor was larger than those assumed by Wigmans in his Monte Carlo simulations, indicating that his results are more optimistic than is the actual case.

As mentioned before, the voltage dependent Birks factor measured in this analysis reflects the voltage dependent difference in the Onsager fit to the proton data. If this is due to a true field dependence in the Birks factor, this feature could be exploited in order to reduce the effective Birks factor

by increasing the external electric field on the liquid.

Jaffé's model did not give consistent fits to the free ion yield data. The pion data seemed to give more reasonable results when modelled alone than when the proton data was included. In comparing these results with those obtained from the G_{fi}^0 values determined from Onsager's formalism, however, the total ion yield densities are significantly different. The data seems to fit Onsager's theory better, suggesting that the problem lies with Jaffé's formalism. Jaffé has noted that his theory did not fit his data well at $\theta = 0^\circ$ which would explain the difficulty in fitting the data in this analysis.

Chapter 6

Conclusions

The ion yields for single ionizing particles in TMP have been measured and have been modelled using two competing ion recombination theories: Onsager's initial recombination theory and Jaffé's columnar recombination theory. The Birks factor has subsequently been determined in Onsager's formalism.

The mobility and lifetime have also been measured giving $\tau_\ell = 411 \pm 200 \mu\text{s}$ and $\mu = 26.0 \pm 1.9 \text{ cm}^2/\text{Vs}$. The large error on the lifetime can be partly attributed to the lack of data for fields which would give $\tau_\ell < t_d$. Li has measured the ion yields and the parameters, μ and τ_ℓ , in TMP using minimum ionizing cosmic rays. He has obtained a mobility of $\mu = 26.3 \pm 0.8 \text{ cm}^2/\text{Vs}$ which agrees with the result presented here.

Onsager's theory has been successfully applied to the free ion yields to determine the zero free ion yield at the three energy deposition values studied. The 400 MeV/c pions used in this analysis are minimum ionizing particles and give a result of $G_{\text{fi}}^0 = 0.768 \pm 0.009(\text{stat.}) \pm 0.077(\text{sys.})$. Li has obtained $G_{\text{fi}}^0 = 0.743 \pm 0.029$ ions/100eV for the minimum ionizing cosmic rays, and

Dodelet and Freeman have determined a zero free ion yield for 1.7 MeV X-rays of $G_{\text{f}}^0 = 0.83$. Both results are consistent with the value measured here.

The problems encountered in modelling Jaffé's theory are not unique. The non-convergence of the proton data was similar to other problems noted by Muñoz's group, by Duhm, Fedder, and Schiffmann [15], and by Jaffé himself. There have been several reasons offered for this discrepancy. Jaffé proposes that, for his data, the angular spread of the incident particles is large enough to increase the observed ion yield. This would not be the case here as the veto counters defined a well collimated beam. Duhm's group proposes that the discrepancy could be due to the approximation of constant ion density instead of using the true Bragg curve description. This effect was accounted for and did not have any significant effect. Finally, Muñoz proposes that secondary electrons, or delta rays, from the ionized track could reduce the effective dE/dx , thus raising the apparent free ion yield. This seems to be a possible explanation in this analysis since this effect would be stronger for higher energy depositions.

The Birks factor for TMP has been measured by Aubert, et. al. at higher fields than were used in this analysis. They modelled their ion yields using simple parameterizations of Onsager's and Jaffé's theories which placed all angular dependence in the Birks factor. They concluded that their parameterization of Jaffé's theory provided a better fit to their data. They obtained lower results for the Birks factor (see Fig. 5.5), but if the apparent voltage dependence indicated in this analysis is correct, the field dependent trend appears to be consistent. An approximate Birks factor can also be determined from the data presented by Holroyd and Sham [16] as $kB \approx 0.10\text{cm/MeV}$ at

an electric field of 5 kV/cm. This, too, appears to indicate that the Birks factor is decreasing with voltage

The apparent voltage dependence in the Birks factor suggests that a systematic study of the response of TMP at higher electric fields may provide an answer to the question of the viability of using TMP in compensating hadron calorimeters. Other studies which could be performed should include a systematic study of the angular dependence of the Birks factor as well as the saturation effects for very high ionization densities. These higher densities could be obtained by allowing the particles to stop within the liquid, but would pose large technical difficulties in accurately determining the theoretical current. The primary difficulty would be in modelling the changing energy deposition. The exact stopping position of the charged particle would need to be very well determined, requiring a very accurate determination of dE/dx . High precision numerical integration of the convolution of the current pulse and the response function would need to be performed. The precision of this integration would thus be limited by the knowledge of dE/dx .

In any further analysis of this type, some other ideas should be kept in mind. The use of the transient analyzer to record the waveforms was quite successful here, but the length of the collection time should be increased in order to provide more channels for digital filtering, and to provide a more consistent response function fit to the waveforms. The free electron lifetime would also be better determined by taking data at lower applied electric fields.

A large first step has been made in determining the response of TMP to highly ionizing particles. The saturation effect of the signal has been parameterized for single particles in a manner that will provide straightforward

input into future calorimeter simulations and prototype designs.

Bibliography

- [1] M.G. Albrow, et.al., Nucl. Instr. and Meth. **A265** (1988) 303.
- [2] R. Wigmans, Nucl. Instr. and Meth. **A259** (1987) 389.
- [3] J.B. Birks, *Theory and Practise of Scintillation Counting*, (Pergammon Press, Oxford, London, New York, Paris, 1964).
- [4] L. Onsager, Phys. Rev., **54** (1938) 554.
- [5] G. Jaffé, Ann. Phys., **42** (1913) 303.
- [6] J.F. Janni, Atomic Data and Nuclear Data Tables, vols. 2/3 and 4/5, Kirtland Airforce Base, New Mexico, 1982.
- [7] L. Landau, J. Phys., **8** (1944) 201-205.
- [8] P.V. Vavilov, JETP, **5** (1957) 749-751.
- [9] B. Schorr, Comp. Phys. Comm. **7** (1974) 215-224.
- [10] G.R. Freeman, J. Chem. Phys. **39** (1963) 1580
- [11] J.P. Dodelet and G.R. Freeman, Can. J. Chem., **50** (1972) 2667.

- [12] Y. Li, M.Sc. Thesis, University of Victoria, 1990.
- [13] B. Aubert, et.al., LAPP-EXP 89/08 (1989) submitted to Nucl. Instr. and Meth.
- [14] R.C. Muñoz, J.B. Cumming, and R.A. Holroyd, J. Chem. Phys. **85** (1986) 1104.
- [15] H.H. Duhm, I. Fedder, and K. Schiffmann, Nucl. Instr. and Meth. **A277** (1989) 565.
- [16] R.A. Holroyd and T.K. Sham, J. Phys. Chem. **89** (1985) 2909.
- [17] R.W. Hamming, *Digital Filters (third edition)*, Prentice Hall, New Jersey, 1989.

Appendix A

Current Pulse - Arbitrary Distribution with Loss

The most general current pulse produced in a material by an ionizing particle is a combination of several terms. Fig. A.1 shows the general configuration of interest in the determination of the pulse shape. A particle enters the chamber at $x = 0$ and passes a distance R at angle θ to the field. The plate at $x = 0$ is electrically neutral and the plate at $x = d$ is at positive voltage, V . The field is thus $E = V/d$, and the drift time of an electron in the material is given by $t_d = d^2/\mu V$, where μ is the mobility of the material.

The charge detected at $x = d$ will be composed of the induced and the collected charges. The collected charge is zero until $t = t_d(1 - R \cos \theta/d)$, so the entire charge detected until then is due to the induced charge. We assume that the initial charge density along the ionization track is given by $\lambda(r)$ where

$$\int_0^R \lambda(r) dr = Ne. \tag{A.1}$$

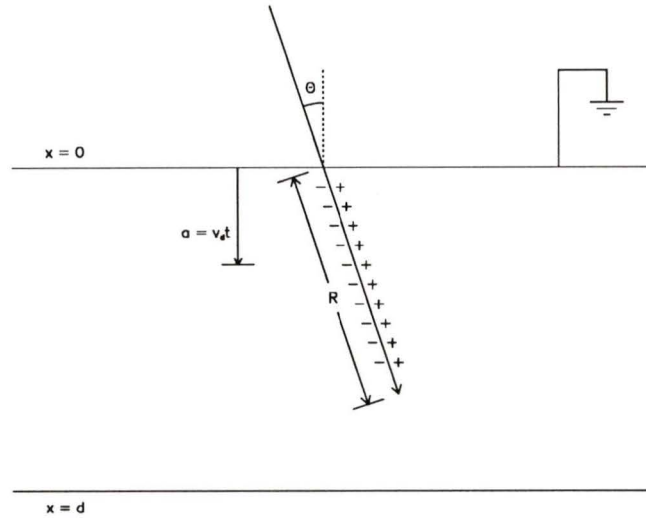


Figure A.1: Ionization chamber track orientation.

The charge induced at $x = d$ by a positive charge at x is

$$q_{\text{ind}}^+(x) = -e \frac{x}{d} \quad (\text{A.2})$$

and so the charge induced by a distribution of positive charges at angle θ and of length R is given by

$$q_{\text{ind}}^+(x = 0 \rightarrow R) = -\frac{\cos \theta}{d} \int_0^R \lambda(r) r dr \quad (\text{A.3})$$

Since the mobility of the positive charges in a liquid is much smaller than that of negative charges, this will be effectively a constant contribution over the time scale of the drift of the negative charges to $x = d$. The total negative charge will, however, be reduced by losses due to impurities trapping the electrons before they have drifted to the positively charged electrode. The distribution of negative charges will therefore be

$$\lambda^-(r, t) = e^{-t/\tau_e} \lambda(r). \quad (\text{A.4})$$

These negative charges will, of course, be drifting towards the positive electrode. If we define a_d as the distance an electron has drifted in time t ($a_d = d(t/t_d)$), then the charge induced by the distribution of negative charges between $x = a_d$ and $x = a_d + R \cos \theta$ is given by

$$q_{\text{ind}}^- (r = [\frac{a_d}{\cos \theta}, \frac{a_d}{\cos \theta} + R], t) = \frac{\cos \theta}{d} \int_{\frac{a_d}{\cos \theta}}^{\frac{a_d}{\cos \theta} + R} \lambda \left(r - \frac{a_d}{\cos \theta}, t \right) r dr \quad (\text{A.5})$$

or

$$q_{\text{ind}}^- (r = [\frac{a_d}{\cos \theta}, \frac{a_d}{\cos \theta} + R], t) = \left(Ne d \frac{t}{t_d} + \frac{\cos \theta}{d} \int_0^R \lambda(r) r dr \right) e^{-t/\tau_\ell}. \quad (\text{A.6})$$

This result can be understood in the following manner. We can effectively replace the positive and negative charge distributions with a single positive and a single negative charge at some point within the cell. The induced charge would be the combination of the induced charge from the stationary positive charge and the negative charge which would be moving toward the positively charged plate. The first term on the right side of Eq. A.6 represents the negative charge associated with the negative ion distribution and the time independent second term in this equation represents the positive charge associated with the stationary positive ion distribution.

The trapped electrons will also contribute to the induced charge at $x = d$. The rate at which electrons are being trapped is

$$\frac{\partial \lambda^-(r, t)}{\partial t} = -\lambda(r) \frac{e^{-t/\tau_\ell}}{\tau_\ell}. \quad (\text{A.7})$$

To calculate the contribution from this term, we need to consider what happens at some position x as time goes from $t = 0$ to $t = \infty$. Two cases

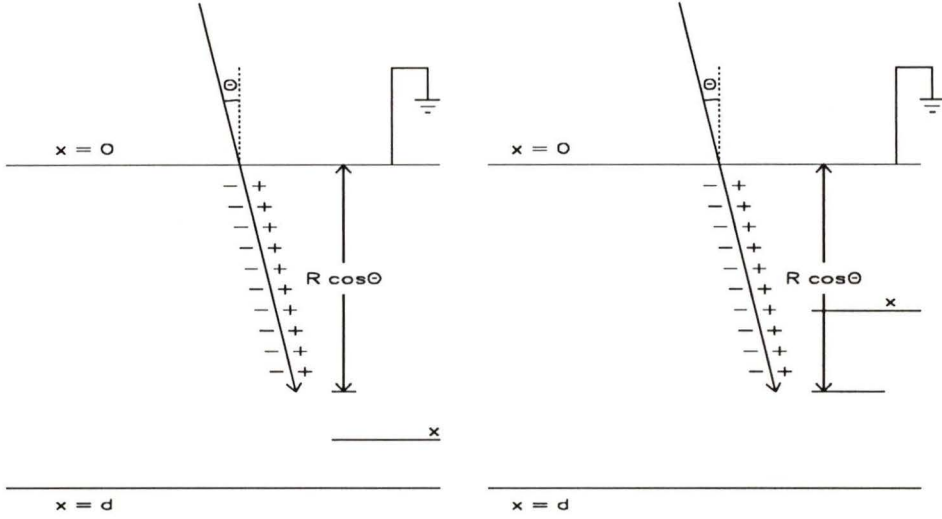


Figure A.2: (a) $x > R \cos \theta$, (b) $x \leq R \cos \theta$.

must be evaluated corresponding to the position x being initially (a) outside and (b) within the charge distribution. From Fig. A.2 we can see that for $x > R \cos \theta$, between $t = 0$ and $t = t_d(x - R \cos \theta)/d$ and after $t = t_d(x/d)$ no more electrons are being trapped at x . Therefore, the integration over time for this x is between $t_d(x - R \cos \theta)/d$ and t until $t = t_d(x/d)$. For $x \leq R \cos \theta$ the upper limit of integration is the same, while the lower limit obviously starts from zero. We can see that we actually have four different cases where the two cases mentioned must be separated into two subcases of $t < t_d(x/d)$ and $t \geq t_d(x/d)$. The density of trapped electrons, $\gamma(x, t)$, is the integral of the rate of trapping given by

$$\gamma(x, t) = -\frac{1}{\tau_\ell} \int \lambda \left(\frac{x - d(t'/t_d)}{\cos \theta} \right) e^{-t'/\tau_\ell} dt' \quad (\text{A.8})$$

and the charge induced by these charges is then

$$q_{\text{ind}}^{\text{trapped}}(t) \equiv T(t) = -\frac{1}{d} \int_0^d \gamma(x, t) x dx. \quad (\text{A.9})$$

The total induced charge before $t = t_d(1 - R \cos \theta/d)$ is then

$$q_{\text{ind}} = Ne \frac{t}{t_d} e^{-t/\tau_\ell} - \frac{\cos \theta}{d} \int_0^R \lambda(r) r dr (1 - e^{-t/\tau_\ell}) + T(t). \quad (\text{A.10})$$

To find the current, we will need to be know the derivative, $dT(t)/dt$. This, in turn, requires knowledge of $d\gamma(x, t)/dt$, which is simply the rate of electron trapping

$$\frac{d\gamma}{dt}(x, t) = \begin{cases} -\lambda \left(\frac{x-a_d}{\cos \theta} \right) e^{-t/\tau_\ell} & ; t < t_d \frac{x}{d} \\ 0 & ; t \geq t_d \frac{x}{d} \end{cases} \quad (\text{A.11})$$

The current can then be reduced to

$$\begin{aligned} i(t) &= \frac{dq_{\text{ind}}}{dt} \\ &= \left\{ Ne \frac{(\tau_\ell - t(1 - \cos \theta))}{t_d} - \frac{\cos \theta}{d} (1 - \cos \theta) \int_0^R \lambda(r) r dr \right\} \frac{e^{-t/\tau_\ell}}{\tau_\ell} \\ &\quad ; t < t_d(1 - R \cos \theta/d). \end{aligned} \quad (\text{A.12})$$

After $t = t_d(1 - R \cos \theta/d)$, negative ions are deposited at $x = d$ at a rate given by

$$\frac{dq_{\text{dep}}}{dt}(t) = -\lambda \left(\frac{d - a_d}{\cos \theta} \right) \frac{d}{\cos \theta} \frac{e^{-t/\tau_\ell}}{t_d}. \quad (\text{A.13})$$

Again, the induced charge due to the positive ions is constant and given in Eq. A.3. The induced charge due to the negative ions is now given by

$$q_{\text{ind}}^-(t) = \frac{\cos \theta}{d} \int_{\frac{a_d}{\cos \theta}}^{\frac{d}{\cos \theta}} \lambda \left(r - \frac{a_d}{\cos \theta}, t \right) r dr \quad (\text{A.14})$$

which reduces to

$$q_{\text{ind}}^-(t) = \frac{t}{t_d} \int_0^{d-a_d} \lambda(x) dx + \frac{\cos \theta}{d} \int_0^{d-a_d} \lambda(x) x dx. \quad (\text{A.15})$$

The trapped electron contribution will still be given by $T(t)$ (Eq. A.9). The total current is now given by the time derivative of the sum of these contributions.

The final form of the current over all times can be summarized as

$$i(t) = \begin{cases} \left\{ Ne^{\frac{(\tau_\ell - t(1 - \cos \theta))}{t_d}} - \frac{\cos \theta}{d} (1 - \cos \theta) \int_0^R \lambda(r) r dr \right\} \frac{e^{-t/\tau_\ell}}{\tau_\ell} & ; t < t_d(1 - R \cos \theta/d) \\ \left\{ \frac{(\tau_\ell - t(1 - \cos \theta))}{t_d} \int_0^{\frac{d - v_d t}{\cos \theta}} \lambda(r) dr - \frac{\cos \theta}{d} (1 - \cos \theta) \int_0^{\frac{d - v_d t}{\cos \theta}} \lambda(r) r dr \right\} \frac{e^{-t/\tau_\ell}}{\tau_\ell} & ; t_d(1 - R \cos \theta/d) < t \leq t_d \\ 0 & ; t \geq t_d. \end{cases} \quad (\text{A.16})$$

In this thesis, we will only be dealing with the case where the incident particle penetrates completely through the cell at an angle $\theta = 0^\circ$. The cell is comprised of two halves (each with width d) with the centre electrode is at a positive high voltage, V . With these assumptions, Eq. A.16 reduces to

$$i(t) = \begin{cases} \left\{ \int_0^{d(1-t/t_d)} \lambda(r) dr + \int_0^{d(1-t/t_d)} \lambda(R - 2d + r) dr \right\} \frac{e^{-t/\tau_\ell}}{t_d} & ; t < t_d \\ 0 & ; t \geq t_d \end{cases} \quad (\text{A.17})$$

where the R in the second term is the true range of an incident particle of the given energy in the material.

Appendix B

Digital Filters

Double pulses and noise can contribute large errors to the determination of the peak heights of each pulse. These contributions were minimized by digitally filtering each waveform. The general theory of digital filters and specific digital filters which were used are explained in more detail in Hamming's book, *Digital Filters* [17].

The first consideration in developing a digital filter is to determine what operations will be performed on the waveforms. This can be more easily understood by Fourier transforming the waveforms and the filter into their frequency representations. This allows the interpretation of the filter as a 'window' which acts on particular frequency regions of the waveforms. Sampling in the time domain causes an effect known as aliasing in the frequency domain. Aliasing occurs when a sinusoid is digitally sampled at a frequency less than twice the frequency of the sinusoid. In this case, the sinusoid will have the same digitized values at the sampling points as a lower frequency sinusoid (see Fig. B.1). The original sinusoid will have a frequency which is an integer multiple of the lower frequency sinusoid. Aliasing can thus be

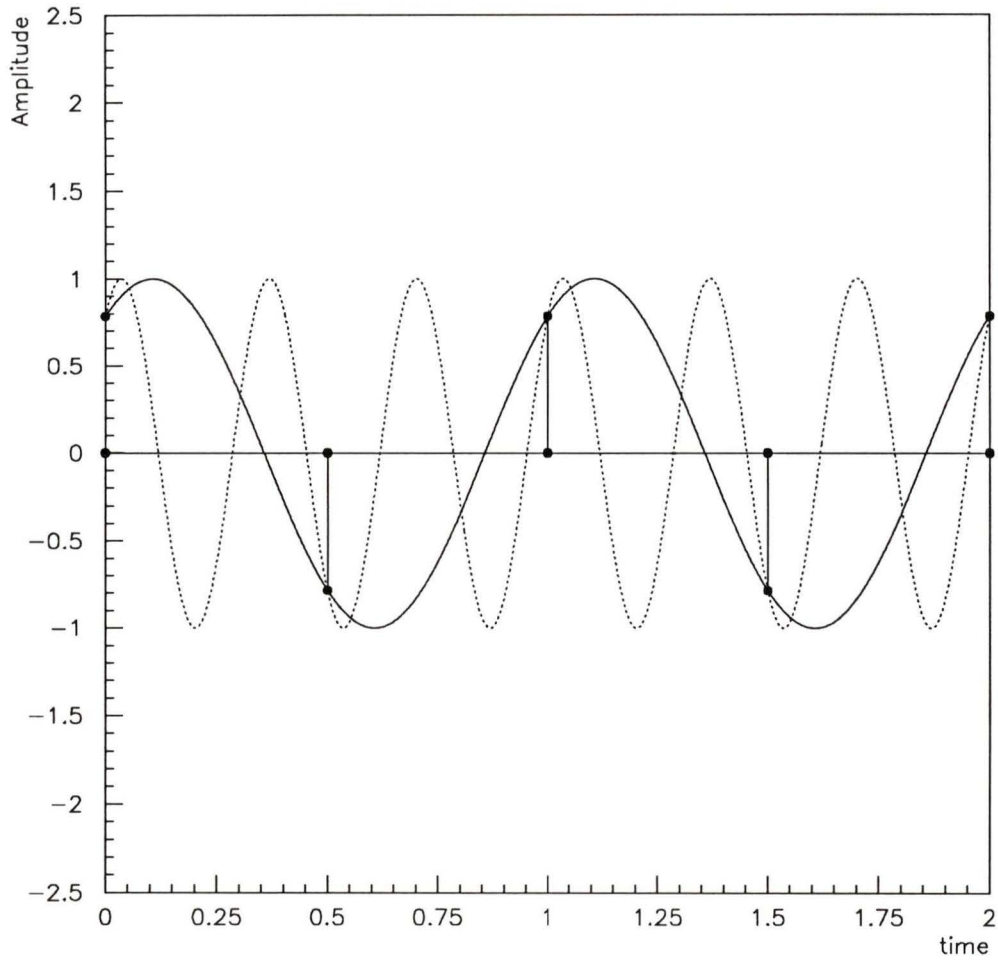


Figure B.1: The sinusoid is sampled at equally spaced intervals. The high frequency and low frequency sinusoids will appear to be identical due to aliasing.

avoided by only studying frequencies which would have at least two samples in each period. This restricts the range of frequencies which can be studied to frequencies lower than the *Nyquist frequency*, defined as one half of the sampling frequency. In this analysis, for example, the waveform is sampled every 400 ns (after the compression discussed in Chapter 4) giving a sampling frequency of 2.5 MHz, and a corresponding Nyquist frequency of 1.25 MHz.

Once the waveform is represented in frequency space, a filter can be designed to act on various regions. Two basic types of filters were eventually chosen for this experiment: a low pass filter and a bandpass differentiator. The low pass filter provided filtering of high frequency noise and the bandpass differentiator differentiated the waveform and removed lower frequency noise.

A digital filter is applied to a waveform by convoluting the filter into the waveform. A non-recursive filter is defined as the convolution of the filter, with coefficients $c_k(-N \leq k \leq N)$, and the waveform, with values u_n at channels n , such that the filtered waveform is given by

$$y_n = \sum_{k=-N}^N c_k u_{n-k}. \quad (\text{B.1})$$

This convolution requires channels at the beginning and the end of the waveform for initialization and termination of the filter. In this analysis, for example, a 21 point window ($N = 10$), a 21 point modified window, and a 141 point bandpass differentiator ($N = 70$) were used. This meant that the first ten channels of the input waveform would be used in ‘initializing’, and the last ten channels in ‘terminating’ each window filter, and 70 channels on either end would be used for the differentiator, for a total of 90 channels

being used on either end of the waveform.

The coefficients of the 21 point window are all $c_k = 1/21$ and the coefficients of the modified window are the same with the exception that $c_{-10} = c_{10} = 1/11.5$. The modified window tends to produce a slightly shifted ripple pattern in frequency space in comparison with the basic window (see Fig. B.2) which, when combined with the basic 21 point window, will cause some cancellation of the undesirable ripples (see Fig. B.3).

The differentiation of the signal was supplied by a bandpass differentiator (Fig. B.4). The limits of the bandpass are generally defined in terms of fractions of the Nyquist frequency. If we define the lower and upper limits as f_p and f_s , respectively, the coefficients of the filter are given by

$$c_k = \left(\frac{\sin \pi k/N}{\pi k/N} \right) \left\{ \frac{2}{k} (f_p \cos 2\pi k f_p - f_s \cos 2\pi k f_s) + \left(\frac{\sin 2\pi k f_s - \sin 2\pi k f_p}{\pi k^2} \right) \right\}. \quad (\text{B.2})$$

The $(\sin \pi k/N)/(\pi k/N)$ term is actually a separate smoothing term (called Lanczos smoothing) which reduces the large ripples in frequency space caused by termination (at $\pm N$) of the Fourier series defining the filter. This effect can be seen in Fig. B.4.

The final filter is defined by the convolution of the three sets of coefficients and is shown in Fig. B.5.

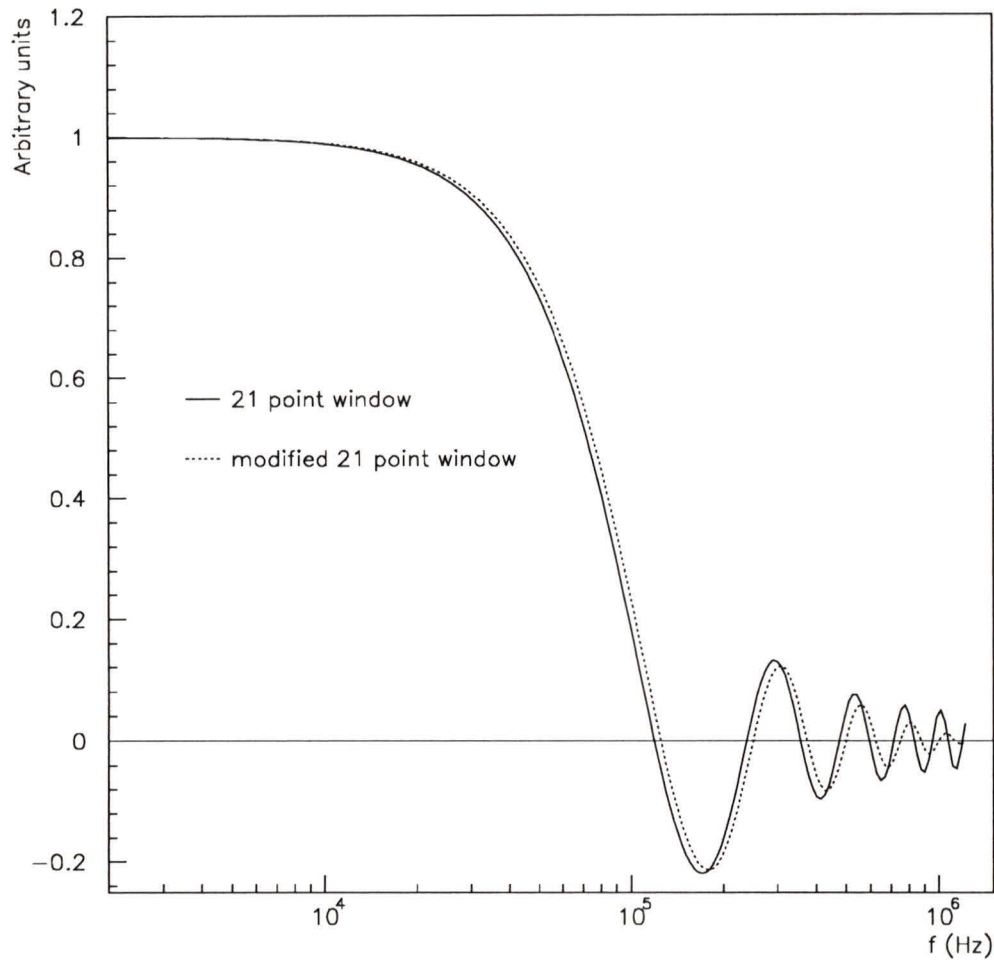


Figure B.2: Frequency space representation of 21 point window filter (solid line) and 21 point modified window filter (dashed line).

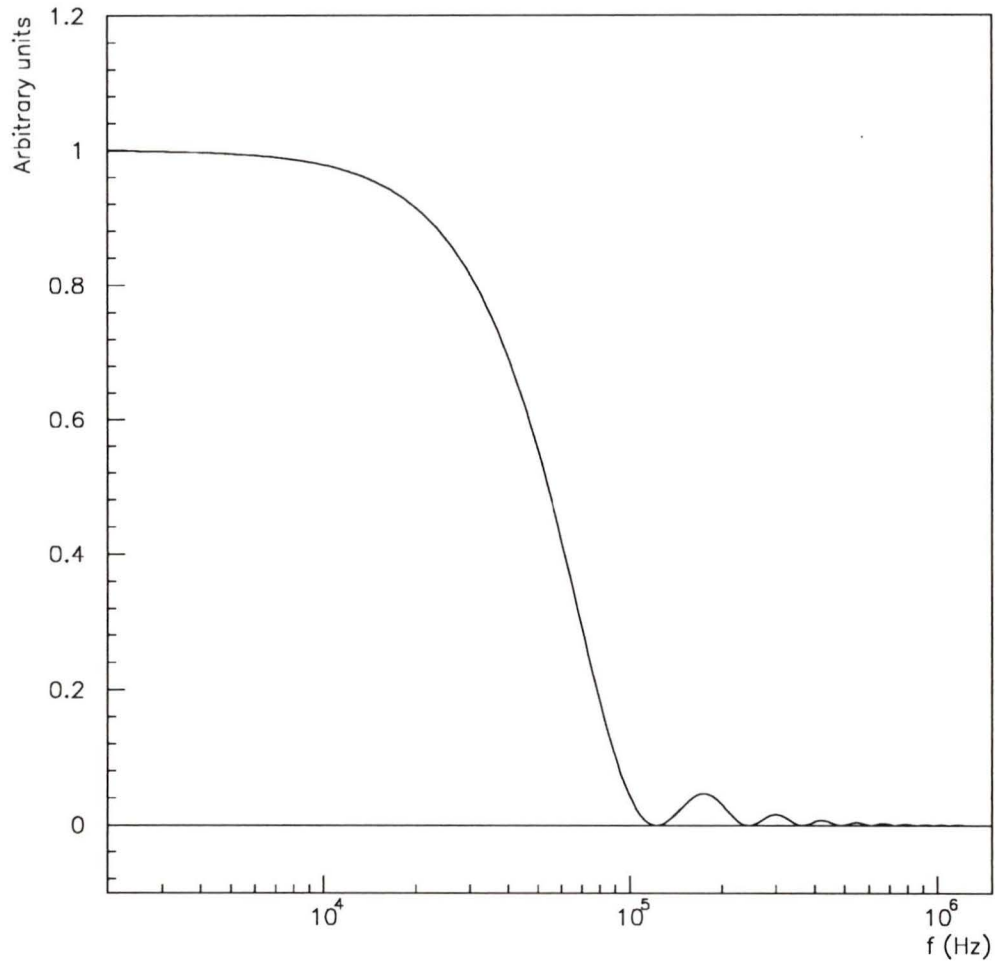


Figure B.3: Frequency space representation of 21 point window filter combined with 21 point modified window.

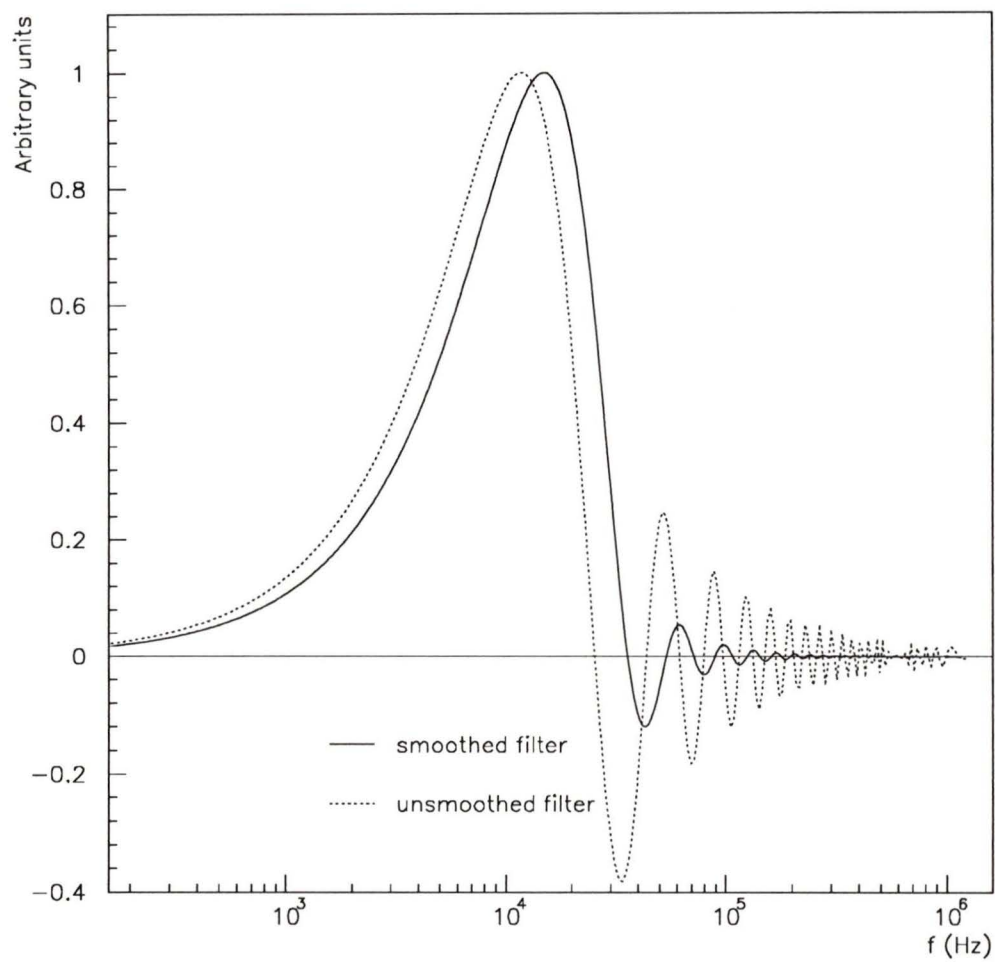


Figure B.4: Frequency space representation of 141 point bandpass differentiator with and without Lanczos smoothing.

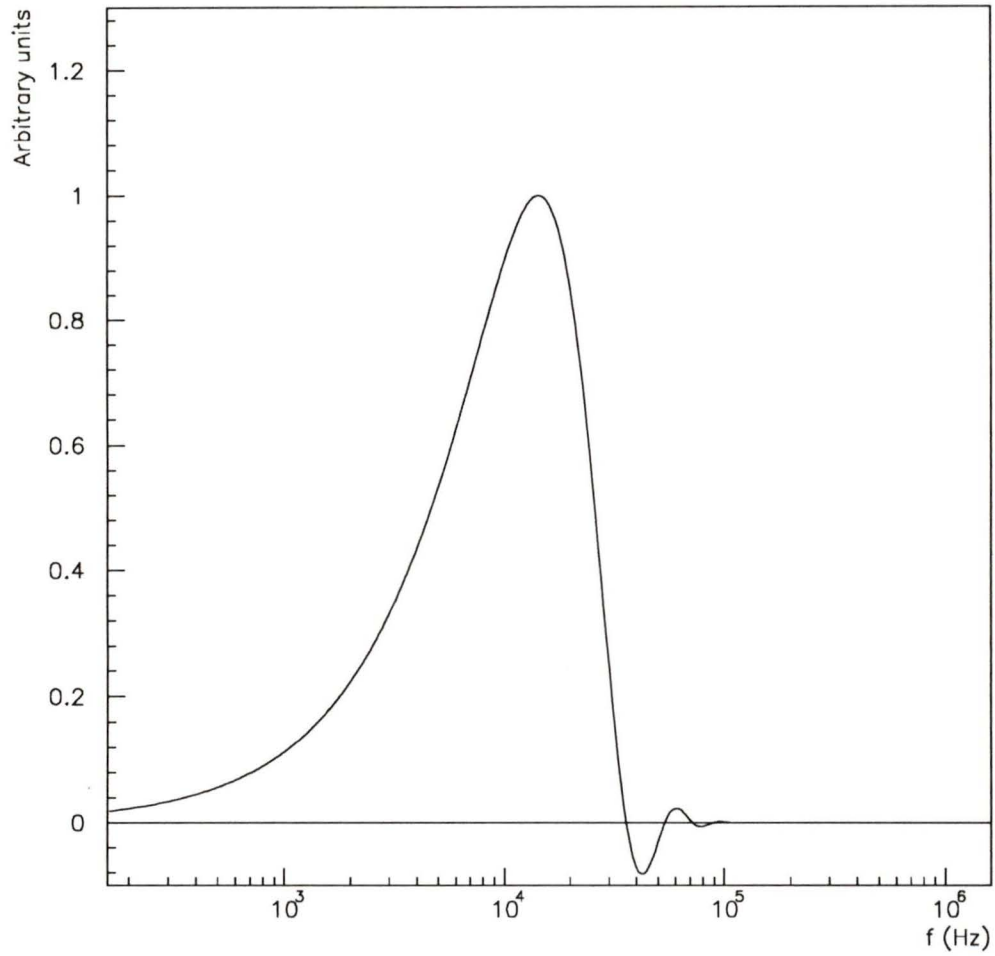


Figure B.5: Full smoothed bandpass differentiating filter.

VITA

Surname: Rosvick
Place of Birth:
Date of Birth:

Given Names: Myron Richard
Lloydminster, Alberta
November 21, 1966

Educational Institutions Attended:

University of Alberta, Edmonton

1984 to 1988

University of Victoria, B.C.

1988 to 1990

Degrees Awarded:

B.Sc. (Honors) 1987 University of Alberta, Edmonton

Honours and Awards:

MacDonnell Graduate Award in Physics

1988 to 1989

The President's Research Scholarship

1990 to 1991

PARTIAL COPYRIGHT LICENSE

I hereby grant the right to lend my thesis (the title of which is shown below) to users of the University of Victoria Library, and to make single copies only for such users or in response to a request from the Library of any other university or similar institution, on its behalf or for one of its users. I further agree that permission for extensive copying of this dissertation for scholarly purposes may be granted by me or a member of the University designated by me. It is understood that copying or publication of this thesis for financial gain shall not be allowed without my written permission.

Title of Thesis:

Saturation of Ion Yield in 2,2,4,4-TMP in Response to
Very Highly Ionizing Radiation



MYRON RICHARD ROSVICK (Author)

NOVEMBER 19, 1990

November 19, 1990